RESEARCH ARTICLE

Endocytosis sustains release at photoreceptor ribbon synapses by restoring fusion competence

Xiangyi Wen[1,2] ⓘ, Matthew J. Van Hook[1] ⓘ, Justin J. Grassmeyer[1,2] ⓘ, Alex I. Wiesman[2] ⓘ, Grace M. Rich[1] ⓘ, Karlene M. Cork[1,2], and Wallace B. Thoreson[1,2] ⓘ

Endocytosis is an essential process at sites of synaptic release. Not only are synaptic vesicles recycled by endocytosis, but the removal of proteins and lipids by endocytosis is needed to restore release site function at active zones after vesicle fusion. Synaptic exocytosis from vertebrate photoreceptors involves synaptic ribbons that serve to cluster vesicles near the presynaptic membrane. In this study, we hypothesize that this clustering increases the likelihood that exocytosis at one ribbon release site may disrupt release at an adjacent site and therefore that endocytosis may be particularly important for restoring release site competence at photoreceptor ribbon synapses. To test this, we combined optical and electrophysiological techniques in salamander rods. Pharmacological inhibition of dynamin-dependent endocytosis rapidly inhibits release from synaptic ribbons and slows recovery of ribbon-mediated release from paired pulse synaptic depression. Inhibiting endocytosis impairs the ability of second-order horizontal cells to follow rod light responses at frequencies as low as 2 Hz. Inhibition of endocytosis also increases lateral membrane mobility of individual Ca²⁺ channels, showing that it changes release site structure. Visualization of single synaptic vesicles by total internal reflection fluorescence microscopy reveals that inhibition of endocytosis reduces the likelihood of fusion among vesicles docked near ribbons and increases the likelihood that they will retreat from the membrane without fusion. Vesicle advance toward the membrane is also reduced, but the number of membrane-associated vesicles is not. Endocytosis therefore appears to be more important for restoring later steps in vesicle fusion than for restoring docking. Unlike conventional synapses in which endocytic restoration of release sites is evident only at high frequencies, endocytosis is needed to maintain release from rod ribbon synapses even at modest frequencies.

Introduction

At presynaptic active zones, the organization of key synaptic proteins influences the efficiency of synaptic vesicle exocytosis. For example, the coupling distance between voltage-gated Ca²⁺ channels and exocytotic Ca²⁺ sensors can give rise to either micro- or nanodomain control of exocytosis (Eggermann et al., 2011), permitting fine adjustments in release kinetics within and between cells (Johnson et al., 2017). Exocytotic fusion of synaptic vesicles results in the addition of lipids and vesicle-associated synaptic proteins to the presynaptic membrane. Compensatory synaptic vesicle endocytosis is needed to retrieve these constituents and replenish vesicle pools for ongoing synaptic transmission. Several studies have also shown that inhibition of endocytosis causes rapid changes in synaptic transmission on timescales several orders of magnitude too fast to be attributable simply to depletion of the synaptic vesicle pool (Kawasaki et al., 2000; Hosoi et al., 2009; Neher, 2010; Hua et al., 2013; Lipstein et al.,

2013; Mahapatra et al., 2016). This implies that endocytosis also plays a key role in homeostasis of the presynaptic active zone by regulating the availability and arrangement of key presynaptic proteins and clearing the active zone of used vesicle fusion machinery (Neher, 2010, 2017). When studied at conventional synapses, this role for endocytosis is evident at high stimulation frequencies of 100 Hz or greater (Lipstein et al., 2013) and may set an upper limit to release rates (Neher, 2017).

Rapid synaptic transmission by rods and cones involves synaptic ribbons, which are protein structures that tether multiple vesicles near the presynaptic membrane and prepare them for exocytosis (LoGiudice and Matthews, 2009; Schmitz, 2009). Rapid, ribbon-mediated exocytosis in photoreceptors is exquisitely sensitive to Ca²⁺, a result of low cooperativity and high affinity for Ca²⁺ in the exocytotic sensor together with nanodomain coupling between Ca²⁺ channels and the synaptic vesicle

[1]Department of Ophthalmology & Visual Sciences, Truhlsen Eye Institute, University of Nebraska Medical Center, Omaha, NE; [2]Department of Pharmacology & Experimental Neuroscience, University of Nebraska Medical Center, Omaha, NE.

Correspondence to Wallace B. Thoreson: wbthores@unmc.edu.

release machinery (Thoreson et al., 2004; Mercer et al., 2011; Van Hook and Thoreson, 2015). This leads to highly efficient coupling between presynaptic Ca^{2+} influx and vesicle exocytosis so that the opening of only a handful of Ca^{2+} channels, less than three in cones and less than five in rods, is needed to release a single synaptic vesicle (Bartoletti et al., 2011; Van Hook and Thoreson, 2015). Hexagonal arrays of vesicles are tethered to photoreceptor ribbons, with the bottom two rows contacting the plasma membrane (Lasansky, 1978; Thoreson et al., 2004; Jackman et al., 2009). The number of vesicles in these bottom two rows corresponds to the size of the physiologically defined, readily releasable pool of vesicles that is released in a synchronous burst by strong depolarizing stimulation (Bartoletti et al., 2010). Neighboring vesicles on the ribbon are separated by as little as 10 nm (Lasansky, 1978; Thoreson et al., 2004). We reasoned that because of the dense packing of vesicles and tight spatial coupling of vesicles and Ca^{2+} channels, the addition of lipids and proteins to the presynaptic membrane from the fusion of a synaptic vesicle might impair the release of a neighboring vesicle, making ribbon-mediated synaptic vesicle exocytosis particularly sensitive to disruption of release site function when endocytosis is inhibited.

In this study, we tested the hypothesis that efficient synaptic transmission by rod photoreceptors requires endocytosis to restore the structural and functional integrity of the presynaptic active zone. This was accomplished by using multiple complementary measures of synaptic function after inhibiting dynamin-dependent endocytosis in rod photoreceptors from tiger salamander retina. Use of large salamander rods allowed us to combine several optical and electrophysiological techniques, including imaging of single Ca^{2+} channel movements, total internal reflection fluorescence microscopy (TIRFM) of vesicle behavior, and whole-cell patch-clamp electrophysiology. We focused on rods because ultrafast endocytosis is more effectively inhibited by use of dynamin inhibitors in rods than in cones (Van Hook and Thoreson, 2012). Synaptic transmission from rods involves fast release from ribbons, amplified by slower release at ectopic sites away from synaptic ribbons driven by CICR from intracellular stores (Krizaj et al., 1999; Cadetti et al., 2006; Suryanarayanan and Slaughter, 2006; Babai et al., 2010; Chen et al., 2013, 2014). We found that inhibition of dynamin-dependent endocytosis reduced the ability of second-order horizontal cells (HCs) to follow rod light responses at modest frequencies. Dynamin inhibition also caused a rapid, modest decrease in release from synaptic ribbons and slowed recovery of ribbon-mediated release from synaptic depression. Inhibition of endocytosis increased the mobility of individual Ca^{2+} channels, providing direct evidence for changes in release site structure. TIRFM techniques provided insights into the behavior of individual synaptic vesicles. In control rods, newly arriving vesicles typically fused soon after descending the ribbon, and membrane-associated vesicles at the ribbon base rarely retreated without fusion. After inhibiting endocytosis, vesicles approaching a ribbon were less likely to fuse, and membrane-associated vesicles were more likely to retreat. Inhibiting endocytosis also impaired the advance of vesicles toward the membrane, but did not impair membrane attachment. These results suggest that endocytosis is more important for restoring functionality of proteins that participate in late stages of vesicle release than in early docking steps. By maintaining the functional organization of the presynaptic active zone, endocytosis is critical for allowing rods to maintain release from ribbon synapses even at low frequencies.

Materials and methods

Animal care and use
Aquatic tiger salamanders (*Ambystoma tigrinum*, 18–25 cm; Sullivan Company) were maintained on a 12-h light/dark cycle and sacrificed after ≥1 h of dark adaptation. Salamanders were anesthetized by immersion in 0.25 g/L Tricaine-S (tricaine methanesulfonate; Western Chemical) for >15 min, decapitated with heavy shears, and then pithed. Procedures were approved by the University of Nebraska Medical Center Institutional Animal Care and Use Committee.

Retinal slices
A detailed description of retinal slice preparation and whole-cell recording techniques has been published previously (Van Hook and Thoreson, 2013). In brief, after enucleation, the front of the eye was removed, and the resulting eyecup was cut into two to four pieces. A piece of retina was placed vitreal side down on a piece of nitrocellulose membrane (5 × 10 mm; type AAWP, 0.8-µm pores; EMD Millipore). The filter paper was then submerged in cold amphibian saline and the sclera peeled away, leaving the retina attached to the membrane. The retina was cut into 125-µm slices using a razor blade tissue slicer (Stoelting). Slices were rotated 90° to view retinal layers and anchored in the recording chamber by embedding the ends of the nitrocellulose membrane in vacuum grease. For light response experiments, slice preparation was performed in darkness using GenIII image intensifiers (Nitemate NAV3; Litton Industries) mounted on a dissecting microscope. For recording, the recording chamber was mounted on an upright fixed-stage microscope (Olympus BH2-WI) and slices were superfused at ~1 ml min^{-1} at room temperature with oxygenated normal amphibian saline solution containing (in mM) 16 NaCl, 2.5 KCl, 1.8 CaCl$_2$, 0.5 MgCl$_2$, 5 glucose, and 10 HEPES, pH 7.8.

Patch-clamp electrophysiology
Patch pipettes were fabricated with borosilicate glass (1.2-mm outer diameter, 0.9-mm inner diameter, with an internal filament; World Precision Instruments) using a PC-10 or PP-830 vertical puller (Narishige). Patch pipettes had tip diameters of ~1 µm and resistances of 10–15 MΩ.

The pipette solution for rods contained (in mM) 50 caesium gluconate, 40 caesium glutamate, 10 TEA-Cl, 3.5 NaCl, 1 CaCl$_2$, 1 MgCl$_2$, 10 ATP-Mg, 0.5 GTP-Na, 10 HEPES, and 5 EGTA. The addition of glutamate to the presynaptic pipette solution enhances postsynaptic currents in HCs during paired whole-cell recording (Bartoletti and Thoreson, 2011). The pipette solution for HC pipettes was identical except that the 40 mM caesium glutamate was replaced with 40 mM caesium gluconate. Reported voltage values were not corrected for a liquid junction potential of 13 mV.

Synaptic transmission was monitored using paired whole-cell recordings from rods and HCs using a Multiclamp 700A

amplifier, pClamp 10.5 software, and a Digidata 1550 digitizer (Molecular Devices). Rods were identified by their morphology. HCs were identified by their morphology, position in the slice, and electrophysiological characteristics (Van Hook and Thoreson, 2013). HCs were voltage clamped at –60 mV and rods at –70 mV. Synaptic vesicle exocytosis from rods was evoked by steps to –10 mV. For measurements of the presynaptic rod Ca^{2+} current (I_{Ca}), leak and capacitative currents were subtracted using a P/8 leak subtraction protocol. We waited at least 1 min between trials to allow recovery.

Rod-driven excitatory postsynaptic currents (EPSCs) involve both fast and slow components. The fastest component involves release from ribbons, whereas the slower component involves nonribbon release triggered by CICR, as well as release from neighboring rods that can be stimulated by spread of depolarizing current through gap junctions (Chen et al., 2014). To minimize release from neighboring rods, trials were performed in the presence of bright white light to hyperpolarize the rod network (Van Hook and Thoreson, 2015).

Light responses of HCs were evoked by sinusoidal modulation of a white light–emitting diode filtered through a 580-nm bandpass filter. The intensity attained at the peak of the sine wave was 19 photons/μm^2/s. A 500-ms, 580-nm flash at this intensity did not produce detectable responses in cones ($n = 3$). Although this intensity was sufficient to evoke measurable HC light responses, rod responses evoked by sinusoidal modulation at this intensity were not large enough for reliable measurement. To measure rod voltage responses, we therefore used a 580-nm sine wave that attained a peak intensity of 340 photons/μm^2/s.

Whole-cell membrane capacitance (C_m) recordings from rods were performed as described previously (Van Hook and Thoreson, 2012; Cork and Thoreson, 2014) using the "track-in" mode of an Optopatch patch-clamp amplifier (Cairn Research). Amplifier output of membrane current, C_m, and access resistance were acquired with pClamp 10.4 software and a Digidata 1322A digitizer (Molecular Devices). The shafts of patch pipettes were coated with dental wax to reduce stray capacitance. The holding potential was varied sinusoidally at ~500 Hz, 30 mV peak to peak, around a holding potential of –70 mV. Output from the phase-lock amplifier was blanked for 3 ms during the test step (–70 to –10 mV, 25 ms) to avoid gating charges, and C_m changes were measured 40 ms after the end of the step. We excluded measurements that showed sizeable poststimulus changes in series resistance.

Reagents
3- and 10-kD dextran-conjugated Alexa Fluor 488 were obtained from Molecular Probes (Invitrogen). Unless otherwise noted, other reagents were from Sigma-Aldrich.

Photoreceptor isolation
For studies on isolated cells, after cutting the eyecup into four pieces, the retina was isolated in Ca^{2+}-free, high-Mg^{2+} amphibian saline consisting of (in mM) 116 NaCl, 2.5 KCl, 5 $MgCl_2$, 5 glucose, and 10 HEPES, pH 7.4. Retinal pieces were incubated with 30 U/ml papain (Worthington) in this Ca^{2+}-free, high-Mg^{2+} saline solution for 35 min at room temperature after activating papain

with 0.2 mg/ml cysteine. To terminate digestion, retinal pieces were transferred to ice-cold, Ca^{2+}-free, high-Mg^{2+} saline supplemented with 1% BSA for 3 min. Retinal pieces were washed for an additional 3 min in ice-cold, Ca^{2+}-free, high-Mg^{2+} saline and then incubated in ice-cold, Ca^{2+}-free, high-Mg^{2+} saline containing DNase (4,000 U/ml; Worthington) for another 5 min. Photoreceptors were isolated by gently triturating retinal pieces ~10 times through the tip of a fire-polished, bent Pasteur pipette. The resulting cell suspension was transferred onto glass coverslips that had previously been coated with 3.5 $\mu g/cm^2$ Cell-Tak (BD Biosciences) and allowed to settle for 20 min. For quantum dot (QD) experiments, we used standard #1 glass coverslips (Warner Instruments). For TIRFM experiments, we used sapphire coverslips with a refractive index of 1.78 (Olympus).

QD binding and imaging
Methods for QD attachment to individual Ca^{2+} channels are described in detail elsewhere (Mercer and Thoreson, 2013). Isolated cells or retinal slices were incubated with a primary anti-$\alpha_2\delta_4$ subunit antibody (1:1,000; Qin et al., 2002) in amphibian saline solution for 3 h at 4°C. Tissue was washed three times with amphibian saline and then incubated for 1 h at 4°C with biotinylated goat anti–rabbit IgG preconjugated to 525- or 625-nm emission QDs (1:2,000; Invitrogen). Tissue was then washed another eight times with amphibian saline and then imaged at room temperature.

The affinity-purified antibody was raised in rabbits (Pacific Immunology) against an amino acid sequence (Ac-KVSDRKFLT PEDEASVC-amide) that exhibits strong homology for $\alpha_2\delta_4$ subunits in several different vertebrates. Specificity of the primary antibody for $\alpha_2\delta_4$ was originally established in human tissue (Qin et al., 2002), but it also labels photoreceptor terminals in the outer plexiform layer (OPL) and bipolar cell terminals in the inner plexiform layer of retinas from salamander, mouse, and zebrafish. This labeling colocalizes with antibody labeling for the synaptic vesicle protein SV2 and the α_1 subunit of $Ca_V1.4$. Labeling was abolished by omission of the primary or secondary antibodies or by coincubation with the peptide against which the antibody was raised (Mercer et al., 2011). Western blots using whole salamander retinal lysate produced a band at 150 kD, as expected for $\alpha_2\delta_4$, and another band at ~130 kD, consistent with dissociated α_2 subunits generated by breaking the disulfide bond under the reducing conditions of the Western blot buffer (Thoreson et al., 2013). $\alpha_2\delta_4$ subunits appear to be linked to the extracellular membrane by a glycosylphosphatidylinositol anchor (Davies et al., 2010; but see Robinson et al., 2011). After incubating isolated cells with phosphatidylinositol (PI)-PLC (3 $\mu g/\mu l$, from *Bacillus cereus*; Sigma-Aldrich) for 1 h at room temperature to cleave the glycosylphosphatidylinositol link, we found that QDs disappeared from 67% (10/15) of QD-labeled terminals. By comparison, only 23% (5/22) of QDs nonspecifically bound to rod inner or outer segments disappeared after treatment with PI-PLC (z test, P = 0.008). These results are consistent with a 50% reduction in cell surface expression of $\alpha_2\delta_4$ expressed in Cos-7 cells after 1–3 h of treatment with PI-PLC (3 $\mu g/\mu l$; Davies et al., 2010).

QDs on isolated rods were visualized on an inverted microscope (Olympus IX71) with a 60×, 1.45 numerical aperture (NA)

oil-immersion objective (Olympus) and cooled electron-multiplying charge-coupled device camera (ImageM-1K, Hamamatsu, ImageEM). Epifluorescence was provided by an X-Cite 120Q light source (Lumen Dynamics Group) with an FITC filter cube and model D122 shutter (UniBlitz). Videos were captured using MetaMorph imaging software (Molecular Devices).

QDs in retinal slices were visualized on an upright fixed stage microscope (Nikon E600FN) through a 60×, 1.2 NA water-immersion objective with correction collar (Nikon) and cooled EMCCD camera (Photometrics) using an FITC filter cube. Videos were captured using NIS-Elements software (Nikon).

QDs were selected for tracking analysis if they were localized to photoreceptor terminals in the OPL or to synaptic terminals of isolated rods and exhibited a small size (≤4 pixels) along with intermittent blinking, consistent with labeling by a single QD (Alcor et al., 2009). Images were smoothed by convolving with a 5 × 5–pixel Gaussian and adjusted to optimize QD contrast. QD position was tracked using NIS-Elements software.

The location of a QD can be determined with precision exceeding the diffraction limit by fitting the fluorescence profile with a Gaussian point spread function (Courty et al., 2006; Alcor et al., 2009). From the SD of displacements exhibited by immobilized QDs, the pointing accuracy (full-width half-maximum = 2.35 × SD) of QDs observed with the 60×, 1.45 NA objective was 46 nm ($n = 10$) and with the 60×, 1.2 NA objective was 72 nm ($n = 32$).

From the x and y coordinates of channel location, we calculated the mean squared displacement (MSD; in micrometers squared per second; Kusumi et al., 1993; Bannai et al., 2006) using the following equation:

$$\text{MSD} = \frac{1}{N-n} \sum_{i=1}^{N-n} \left[(X_{i+n} - X_i)^2 + (Y_{i+n} - Y_i)^2 \right]. \quad (1)$$

We measured the confinement area that a given Ca^{2+} channel traverses within the presynaptic plasma membrane by fitting the data with Eq. 2 (Kusumi et al., 1993; Bannai et al., 2006):

$$\text{MSD} = \frac{L^2}{3} \left[1 - \exp\left(\frac{-12Dt}{L^2} \right) \right]. \quad (2)$$

In this equation, L^2 provides the surface area that a given channel traverses, and D is the diffusion coefficient for movements before confinement. Channel movements in the z plane could not be tracked, so these confinement areas represent lower bounds of the true values (Hall, 2008).

TIRFM experiments
TIRFM experiments were performed as described previously (Chen et al., 2013; Wen et al., 2017). A solid-state laser (561 nm; Melles Griot) was focused off-axis through the objective (100×, 1.65 NA oil immersion; Olympus) so that the beam underwent total internal reflection at the interface between the coverslip and the overlying cell membrane or aqueous solution. We used an incident angle of ~60° that generates an evanescent wave with length constants of ~65 nm and ~57 nm for 561- and 488-nm lasers, respectively (Chen et al., 2013; Wen et al., 2017). Fluorescence emission was collected through 609-nm bandpass filters (54 nm wide; Semrock) and 525-nm bandpass filters (45 nm

wide; Semrock) using an EMCCD camera (Hamamatsu) at 40 ms/frame with a pixel size of 80 nm/pixel.

To load synaptic vesicles of rods with fluorescent dye, tissue was dissected and retinas were isolated in darkness using GenIII image intensifiers mounted on a dissecting microscope. Maintaining retinae in a dark-adapted state keeps photoreceptors at a depolarized resting membrane potential of approximately –40 mV and thus promotes vesicle cycling. Retinal pieces were incubated with either 3-kD Alexa Fluor 488 (400 µg/ml) for 1.5 min or 10-kD Alexa Fluor 488 (500 µg/ml) for 3 min. We have found that the lower background membrane staining observed with fluid phase indicators compared with lipophilic dyes such as FM1-43 yields a better signal-to-noise ratio (Chen et al., 2013). Use of short incubation times loads only a small percentage of vesicles (Chen et al., 2013; Wen et al., 2017).

For some TIRFM experiments, synaptic vesicle release was stimulated by depolarizing rod terminals with a 2-s puff of 50 mM KCl. For puff application, a glass patch pipette was filled with 50 mM KCl amphibian saline containing (in mM) 68.6 NaCl, 50 KCl, 1.8 $CaCl_2$, 0.5 $MgCl_2$, 5 glucose, and 10 HEPES, pH 7.8, and connected to a pressure valve system (8 psi; Toohey Company). The tip of the puffer pipette was positioned 10–20 µm away from rod terminals. For other experiments, we stimulated release by applying depolarizing voltage steps (–70 to –10 mV, 100 ms) to voltage-clamped, isolated rods. In some, we also introduced a fluorescent Ribeye-binding peptide (tetramethylrhodamine-EQTVPLDLSKRDR; Biomatik; 50 µM) through the pipette (Zenisek et al., 2004; Francis et al., 2011). We measured the distance from the center of each vesicle to the edge of the nearest ribbon. We constructed the relative frequency histogram of events using a bin size of 350 nm, matching the optical point spread function measured with this objective (Chen et al., 2013). We calculated the radial density distribution using the following formula:

$$d(r) = N(r) / \pi \left[\left(r + \frac{n}{2} \right)^2 - \left(r - \frac{n}{2} \right)^2 \right], \quad (3)$$

where r is the radial distance to the center of each bin, n is the bin size (350 nm), and $N(r)$ is the number of events in each bin.

Data were acquired and analyzed using MetaMorph software. Only vesicles showing a signal-to-noise ratio four times more than the peak-to-peak baseline noise within a 7 × 7–pixel region of interest were selected for analysis. As described in detail elsewhere (Chen et al., 2013; Wen et al., 2017), kinetic differences between vesicle appearance during advance and vesicle disappearance were used to distinguish release events from nonrelease events where vesicles depart the membrane without fusion. If a vesicle departs without fusion, then its fluorescence should decline at a rate similar to the increase in fluorescence that accompanies advance of the vesicle toward the membrane as it moves through the exponentially increasing evanescent field. If a vesicle fuses and releases its contents, then its fluorescence will decline almost instantaneously. To be defined as a release event, we required that vesicle fluorescence fall to <40% of the original peak fluorescence in the first 40-ms frame during the decline phase and to baseline levels by the second frame (Chen et al., 2013). Fusion events that fulfill these criteria showed release kinetics matching those measured by capacitance techniques and were blocked by Co^{2+} or Cd^{2+},

confirming that a majority of these events were caused by Ca^{2+}-dependent release (Chen et al., 2013; Wen et al., 2017; present study).

Statistical analysis
Most statistical analyses were performed using Prism 4.0 (GraphPad Software), and results are presented as mean ± SEM. Z tests were performed using an online calculator (http://www.socscistatistics.com/tests/ztest_sample_mean).

Results
Sinusoidally modulated HC light responses are attenuated by dynasore
To examine the requirement for endocytosis in sustaining release at rod synapses, we tested whether inhibiting endocytosis with a small molecule inhibitor of dynamin, dynasore, alters the ability of HCs to follow responses of rods to sinusoidally modulated light. We selected rods for these experiments because fast endocytosis is blocked more effectively in rods than in cones by inhibiting dynamin or GTPase activity (Van Hook and Thoreson, 2012). We recorded voltage responses from dark-adapted rods and light-evoked currents from dark-adapted HCs evoked by sinusoidal modulation of dim 580-nm light. A 500-ms, 580-nm flash equal to the peak intensity of the sine wave used to evoke HC responses (19 photons/μm^2/s) did not evoke detectable responses in cones ($n = 3$). Because of nonlinearities in the light-emitting diode, the light was not perfectly sinusoidal, and so we performed power spectral analysis to extract the power of the response at stimulation frequencies of 1, 2, 4, and 8 Hz. Responses were normalized to the power measured at 1-Hz stimulation. HC light responses showed bandpass characteristics with a peak response at 2 Hz (Fig. 1 B). Light-evoked voltage responses of rods did not show these bandpass features (Fig. 1 D) that arise at the rod synapse by signal spread through the network of coupled rods (Armstrong-Gold and Rieke, 2003). The transmission of light-evoked currents in HCs at 2 Hz was diminished significantly by bath application of dynasore (80 μM; P = 0.042, paired t test; control, $n = 11$; dynasore, $n = 11$; Fig. 1, A and B). The power at 2 Hz and concomitant bandpass characteristics recovered after washout (wash, $n = 9$). HC responses diminished substantially at 4 and 8 Hz, obscuring possible effects of dynasore at these frequencies. We observed a slight increase in the power of rod light responses with dynasore, but this did not attain statistical significance at 2 Hz (normalized power at 2 Hz, $n = 10$; P = 0.23, paired t tests; Fig. 1, C and D) or any other frequency. Furthermore, an increase in rod light responses would be expected to increase, not decrease, HC light responses. Rod resting membrane potentials also did not differ significantly in control (−39.7 ± 3.73 mV, $n = 10$) and dynasore (−38.9 ± 3.41 mV; P = 0.68, paired t test) conditions. The reduction in the ability of HCs to follow rod responses at 2 Hz therefore suggests a role for endocytosis in allowing rod synapses to maintain signaling under conditions of changing illumination, even at modest frequencies. Changes in response power amplitude at 1 Hz were not statistically significant (P = 0.28), suggesting that this was not caused by a substantial overall reduction in the amount of release, as might result from vesicle pool depletion. In contrast with results at rod ribbon synapses, disruption of release site

function at conventional synapses induced by inhibition of endocytosis is apparent only at high stimulation frequencies (Lipstein et al., 2013).

Inhibition of endocytosis in rods by dynasore inhibits release
To examine the impact of endocytosis on synaptic release more directly, we bath applied dynasore (80 μM) while recording EPSCs of HCs evoked by depolarizing steps applied to simultaneously voltage-clamped rods in retinal slices (Fig. 2). The initial fast component of HC EPSCs evoked by depolarizing steps applied to a rod (Fig. 2 A, arrow) results from ribbon-mediated release (Chen et al., 2013, 2014). Fast, ribbon-mediated release is followed by a second, slower EPSC component that involves ectopic release at nonribbon sites driven by CICR (Chen et al., 2013, 2014). There is also a contribution to slower components of the EPSC that is caused by release that can be evoked by spread of depolarizing current through gap junctions to neighboring rods (Cadetti et al., 2005). We minimized the contribution of this component by recording EPSCs in the presence of a bright white light that hyperpolarizes neighboring rods and thus limits the impact of any currents that might spread through gap junctions (Van Hook and Thoreson, 2015). As illustrated by the example in Fig. 2 A, the first EPSC evoked after dynasore reached the bath showed an immediate reduction in the amplitude of the fast, ribbon-mediated component but not the slower component that results largely from exocytosis at nonribbon sites (Chen et al., 2013, 2014). With continued application of dynasore, the slower component also declined (Fig. 2 A, rightmost response). The presynaptic L-type I_{Ca} that mediates release from rod terminals was not inhibited by dynasore treatment. Fig. 2 B plots data from a subset of rod/HC pairs in which we continued dynasore application for an extended time period. In this graph, the amplitudes of fast, ribbon-related EPSCs were normalized to earlier control amplitudes (mean of the first four responses in control conditions). In control recordings conducted without dynasore, fast ribbon-mediated EPSCs typically increased during the first few minutes of recording (Fig. 2 B, shaded circles) as a result of introducing 40 mM glutamate into the rod through the patch pipette (Bartoletti and Thoreson, 2011). This was followed by a protracted rundown of fast, ribbon-mediated EPSC components. Perhaps because of this rapid rundown, we did not observe recovery of fast EPSC components after washout when dynasore was applied for periods of only 3–5 min. Because of perfusion line delays, dynasore reached the retina ~40 s after starting bath application. In the sample of cell pairs with prolonged application of dynasore, EPSCs declined during the first 1–2 min of dynasore treatment (control, $n = 10$; dynasore, $n = 14$). However, these effects were small, and the differences between control and dynasore-treated pairs were not statistically significant after correcting t tests for multiple comparisons. After this initial decline, the rate at which fast EPSCs declined in dynasore-treated tissue paralleled the rate of rundown in control cells.

In control cell pairs, slow EPSC components showed little rundown over the first 12 min of recording (Fig. 2 C, shaded circles). However, after application of dynasore, slow components showed a gradual decline that differed significantly from control slices (Fig. 2 C; P = 0.0054, ANOVA comparing responses measured 7–11 min after starting dynasore application).
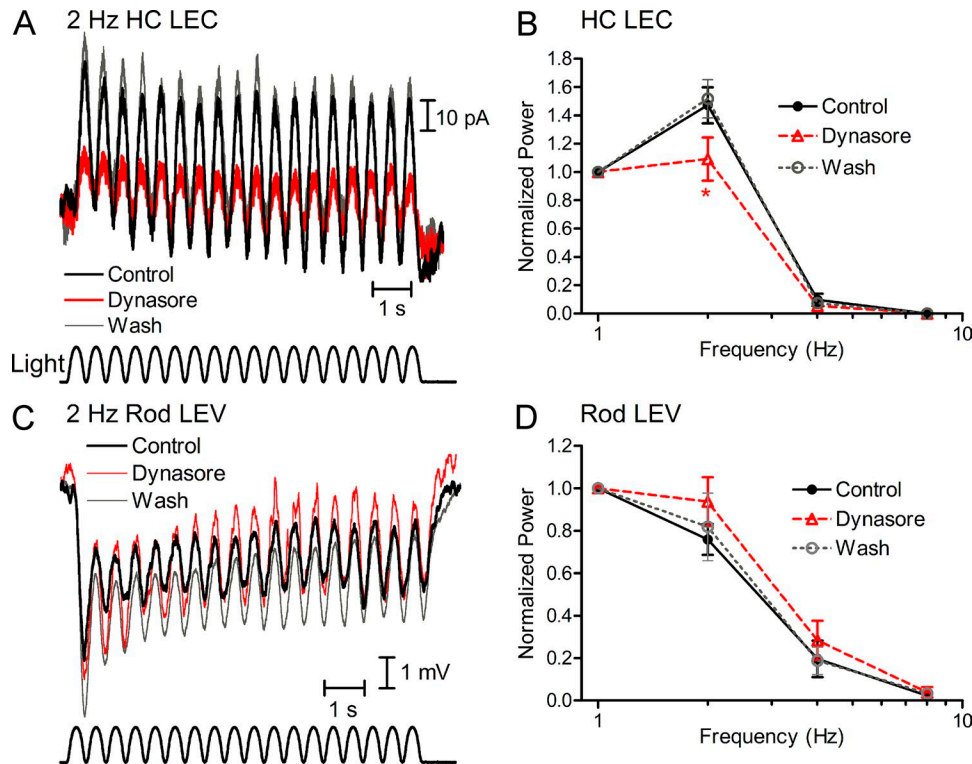
Figure 1. Dynasore treatment impaired the ability of HCs to follow rod light responses. (A) An example of light-evoked currents (LEC) recorded from a dark-adapted HC while sinusoidally modulating a dim 580-nm light (19 photons/μm^2/s) at 2 Hz to record rod-driven responses. The HC light response diminished during bath application of dynasore (80 μM) and then recovered after washout. **(B)** Power of HC light-evoked currents normalized to response power measured at 1-Hz stimulation. The enhancement of light-evoked currents in HCs at 2 Hz and attendant bandpass characteristics were diminished significantly by bath application of dynasore (P = 0.042, paired t test; control, n = 11; dynasore, n = 11). Responses recovered after washout (wash, n = 9). **(C)** Example of light-evoked voltage (LEV) responses from a rod evoked by 2-Hz modulation with 580-nm light (340 photons/μm^2/s). **(D)** Response power of light-evoked voltage responses of rods normalized to the power measured at 1 Hz. Rod responses were not significantly affected by dynasore treatment (control, n = 10; dynasore, n = 10; wash, n = 7). Error bars represent ±SEM.

Because these experiments suggested that maximal effects on the fast EPSC component were attained within 2 min of dynasore application, we made paired comparisons within rod/HC pairs between control responses and test responses measured in the first 2 min of dynasore application. The control responses in Fig. 2 B suggest that there was minimal rundown during the first 2 min of dynasore application. For these comparisons, we used all of the cell pairs, including those in which dynasore was applied for only 3 min. These comparisons showed a small but significant reduction in fast EPSC components (Fig. 2 D, dynasore/control: 0.82 ± 0.038, n = 22; P = 0.0001, one sample t test) but no significant change in slower EPSC components (dynasore/control: 1.03 ± 0.059, n = 23; P = 0.61) or presynaptic I_{Ca} (0.995 ± 0.022, n = 20; P = 0.83). Consistent with previous findings (Van Hook and Thoreson, 2012), bath application of dynasore also inhibited the amplitude of exocytotic capacitance jumps evoked in rods by 25-ms depolarizing steps to −10 mV (control, 52.7 ± 8.05 fF, n = 12; dynasore, 31.0 ± 5.67 fF, n = 11; P = 0.042, unpaired t test).

We also recorded spontaneously occurring miniature EPSCs (mEPSCs) in HCs during prolonged dynasore treatment. Fig. 2 E shows examples of mEPSCs recorded from an HC while a presynaptic rod was voltage clamped at −70 mV. Some of these mEPSCs were caused by Ca^{2+}-dependent release by neighboring photoreceptors that remained sufficiently depolarized in these light-adapted preparations to allow Ca^{2+} channel openings. Other mEPSCs were caused by Ca^{2+}-independent spontaneous release (Cork et al., 2016). Neither frequency (Fig. 2 F) nor amplitude (Fig. 2 G) of spontaneous mEPSCs were significantly reduced during an 8-min bath application of dynasore. This suggests that the cytoplasmic reserve pool of vesicles involved in spontaneous release was not significantly depleted by inhibition of endocytosis during this time period.

These results suggest that dynasore can cause a small degree of inhibition of fast, ribbon-mediated release even when the presynaptic rod is voltage clamped at −70 mV to prevent Ca^{2+}-dependent synchronous release of vesicles before the first test pulse. The speed with which dynasore inhibited postsynaptic responses in the absence of significant prior synaptic release suggests that its inhibitory effects were not simply caused by impaired refilling of the releasable pool of vesicles. This interpretation is supported by differences in the time course of inhibition between fast, slow, and spontaneous release (although such differences could also be explained by involvement of three distinct vesicle pools in these three modes of release). These results further suggest that even the few spontaneous release events that occur in rods voltage clamped at −70 mV (Cork et al., 2016) may be sufficient to disrupt the organization and function of ribbon release sites when compensatory endocytosis is inhibited.
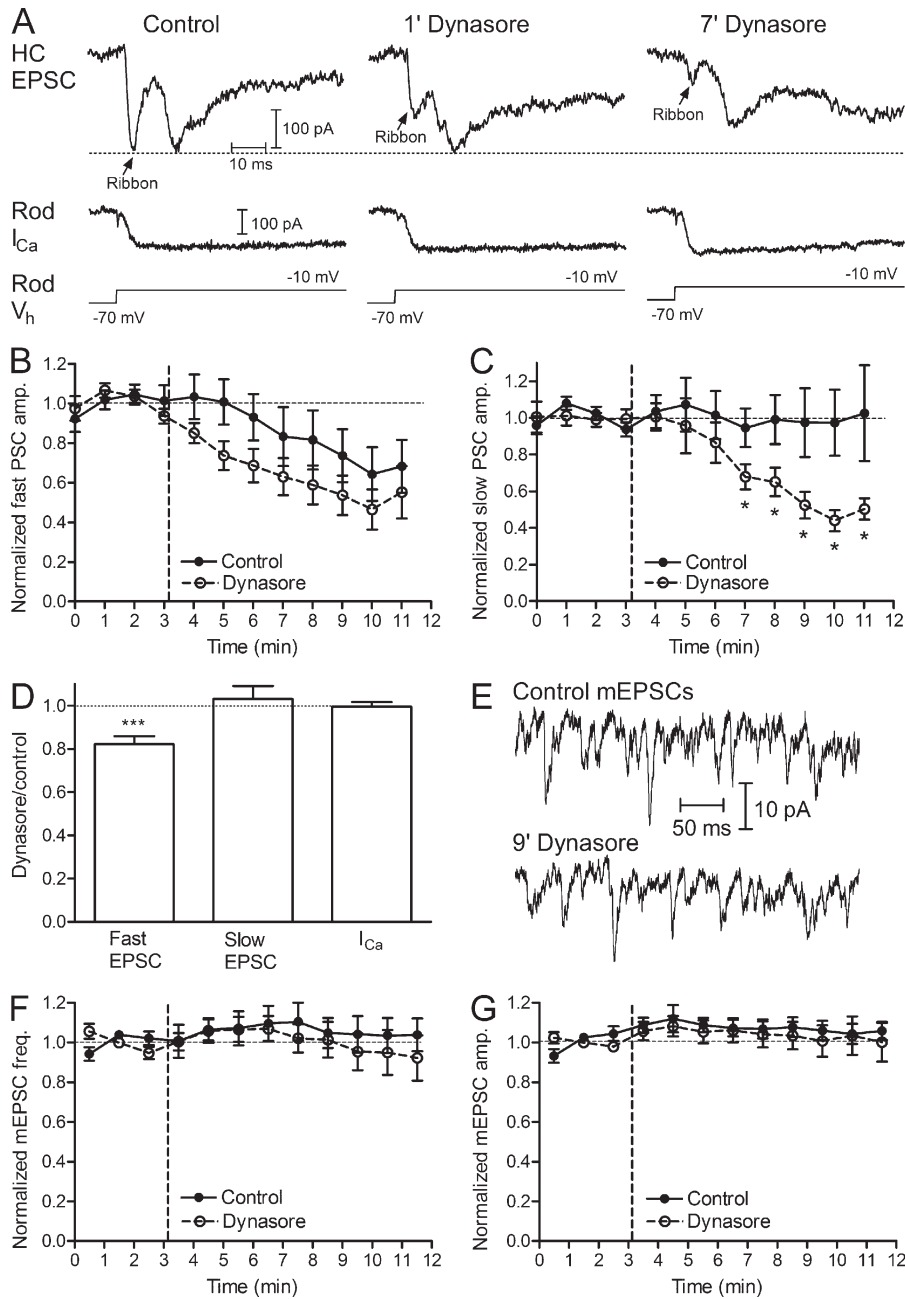
Figure 2. **Inhibition of endocytosis with dynasore caused an immediate decline in fast, ribbon-related components of EPSCs but not slower components. (A)** Top traces: EPSCs recorded from an HC voltage clamped at –60 mV evoked by a 200-ms depolarizing step from –70 to –10 mV. Bottom traces: I_{Ca} recorded simultaneously in the presynaptic rod. Passive currents were removed by P/8 subtraction of the rod membrane current. The voltage changes applied to the rod are shown at the bottom (Rod V_h). The first pair of traces at the left were obtained in control conditions, and the second pair of traces were obtained 60 s later with no intervening stimulation after starting application of dynasore (80 µM). The third pair of traces was obtained after a 7-min application of dynasore. **(B)** Maintained application of dynasore (80 µM) caused an initial rapid decline in the fast component of HC EPSCs. The graph plots the amplitude of fast, ribbon-mediated EPSCs as a function of time. Responses were normalized to the mean amplitude measured during the first four control EPSCs in both control ($n = 10$) and dynasore-treated retinas ($n = 14$). **(C)** Slow EPSC components showed a more gradual decline in amplitude. Slow EPSCs in dynasore-treated rod/HC pairs ($n = 14$) declined more rapidly than control responses ($n = 13$). These differences attained statistical significance 7–11 min after beginning application of dynasore (*, P = 0.0054, ANOVA; control, $n = 14$; dynasore, $n = 13$). **(D)** Paired comparisons between control responses and test responses obtained within 1–2 min of dynasore application. Test responses obtained after dynasore treatment were normalized to the amplitude of prior control responses in the same cell pair. Experiments in which dynasore was applied for both short and long periods were included in this comparison. Fast EPSCs were significantly inhibited (dynasore/control: 0.82 ± 0.038, $n = 22$; ***, P = 0.0001, one sample t test), but there was no significant change in slower EPSC components (dynasore/control: 1.03 ± 0.059, $n = 23$; P = 0.61) or presynaptic I_{Ca} (0.995 ± 0.022, $n = 20$; P = 0.83). **(E)** Examples of spontaneous mEPSCs recorded from an HC in control conditions and after 9 min of treatment with dynasore. **(F and G)** Plots of the frequency (F) and amplitude (G) of mEPSCs normalized to the first three control responses (control, $n = 10$; dynasore, $n = 11$). The vertical dashed lines show the time that dynasore application was started. Error bars represent ±SEM.

Paired pulse depression is extended by inhibiting endocytosis
If inhibition of ribbon-mediated release by dynasore results from impaired clearance of ribbon release sites and a consequent disruption of active zone function, then this should impair replenishment of the releasable vesicle pool. Impaired replenishment should in turn result in slower recovery from paired pulse depression of fast, ribbon-mediated EPSCs at rod synapses (Rabl et al., 2006; Innocenti and Heidelberger, 2008). We tested this prediction by applying pairs of depolarizing pulses (100 ms) separated by varying interpulse intervals to rods while recording EPSCs from a simultaneously voltage-clamped HC.

The paired pulse protocol is illustrated for a control rod/HC pair in Fig. 3 A. We focused primarily on the fast, ribbon-mediated component of release (Fig. 3, arrows). At the beginning of the trial, the readily releasable pool of vesicles at the ribbon base was emptied by applying a brief depolarizing pulse (100 ms to –10 mV) to the rod. In this control cell pair, after waiting 0.5 s, the same test pulse evoked a fast, ribbon-mediated component that was ∼40% of the original response, indicating that ∼40% of the readily releasable pool had recovered within that 0.5-s interval. We tested the effects of three different dynamin inhibitors on recovery from paired pulse depression: dynasore (80 µM;

Fig. 3 B); a more potent dynasore analogue, dyngo-4A (30 µM; Abcam; Fig. 3 C; McCluskey et al., 2013); and a peptide that inhibits dynamin-dependent endocytosis by binding to a proline-rich region of dynamin (1 mM, QVPSRPNRAP; Tocris; Fig. 3 D; Grabs et al., 1997; Jockusch et al., 2005). To avoid the potential for postsynaptic effects, we introduced these inhibitors into individual rods through the presynaptic patch pipette. To allow sufficient time for compounds to diffuse from the patch pipette to the synapse, we waited at least 7 min after rupturing before beginning measurements (Van Hook and Thoreson, 2014). With all three dynamin inhibitors, there was significantly less recovery of the fast, ribbon-mediated component of release compared with control after an interpulse interval of 0.5 s (vehicle control [0.1% DMSO], $n = 10$; dynasore, $n = 15$; P = 0.0082, unpaired t test; dyngo-4A, $n = 10$; P = 0.0025; dynamin inhibitory peptide [DIP], $n = 7$; P = 0.0029). DIP also significantly reduced recovery after 1-s interpulse intervals (P = 0.0195), but the effects of dyngo-4A (P = 0.0565) and dynasore (P = 0.1454) did not attain statistical significance. The significant inhibition of synaptic recovery in HCs after an interval of 0.5 s is consistent with significant inhibition of HC light responses observed at 2 Hz.

We varied the interpulse interval to measure the rate at which EPSCs recovered. This recovery is largely caused by vesicle replenishment (Rabl et al., 2006). Recovery of fast, ribbon-mediated EPSCs was fit with a double exponential function (Fig. 4 A). For clarity, data obtained with shorter interpulse intervals are replotted in Fig. 4 B at higher magnification; data points for dyngo-4A were also nudged by +0.1 s in Fig. 4 B to avoid overlap. Under control conditions, the fast time constant for recovery from paired pulse depression averaged 618 ms (Fig. 4, A and B), similar to fast time constants for recovery from paired pulse depression of ribbon-mediated release at salamander cone ribbon synapses (663–815 ms; Van Hook et al., 2014; Thoreson et al., 2016). The fast time constant for recovery from paired pulse depression of ribbon-mediated EPSCs slowed from 618 ms to 2.5 s after introducing dynasore into presynaptic rods (Fig. 4, A and B). Introducing the more potent inhibitor dyngo-4A or DIP slowed recovery further to 3.2 s and 3.1 s, respectively (dyngo-4A, P < 0.001, F test; DIP, P = 0.0003). Although dynasore and its analogue dyngo-4A may have effects on other mechanisms (Douthitt et al., 2011; Girard et al., 2011; Park et al., 2013; Preta et al., 2015), these are not likely to be shared with DIP, and so the finding that all three inhibitors produced similar effects argues that the slowing of replenishment was caused by inhibition of dynamin-mediated endocytosis.

We also examined recovery from paired pulse depression for slower EPSC components that are largely caused by nonribbon release. When there was not a distinct second peak in the EPSC, we measured the mean amplitude of the EPSC at the end of the test step. Recovery from paired pulse depression of slow EPSC components was fit with a single exponential. Time constants for recovery did not differ significantly between rods treated with vehicle control, dynasore, dyngo-4A, or DIP (Fig. 4 C). Thus, unlike fast ribbon-mediated release, the recovery of slow release was not prolonged by inhibition of endocytosis.

Presynaptic I_{Ca} charge transfer (Q_{Ca}) showed a modest paired pulse facilitation and not paired pulse depression with short
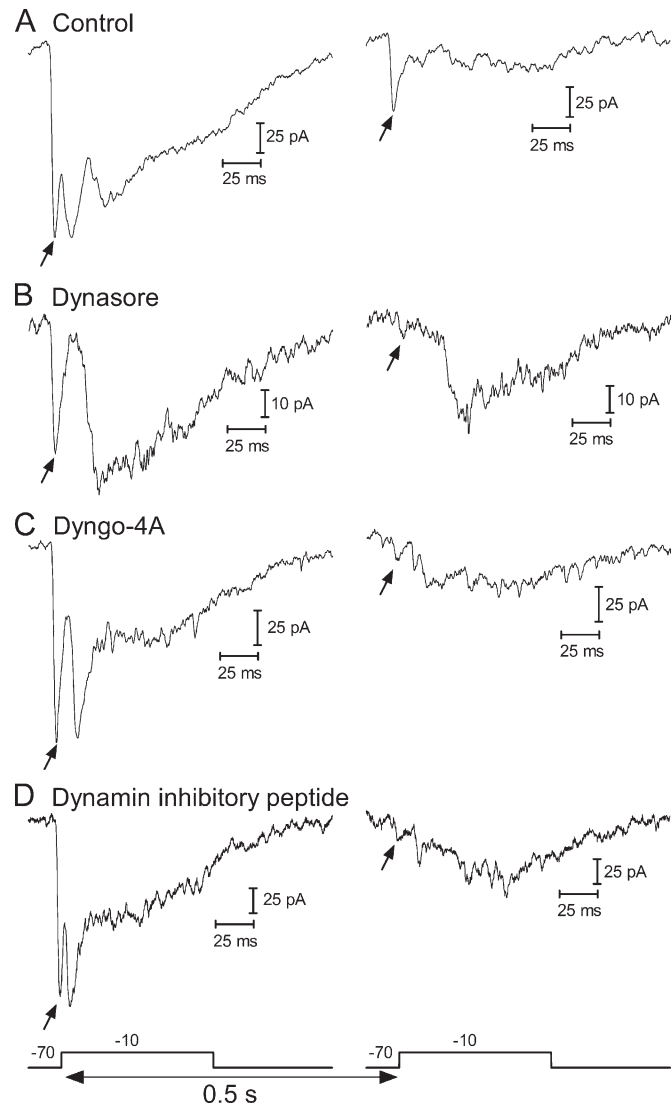

Figure 3. **Examples of recovery from paired pulse depression of EPSCs evoked in HCs by depolarizing steps (–70 to –10 mV, 50 ms) applied to simultaneously voltage-clamped rods.** In the left column are initial control EPSCs, and in the right column are the EPSCs evoked after an interpulse interval of 500 ms. The stimulus protocol is illustrated at the bottom of the figure. **(A)** The fast, ribbon-related component (arrows) of the EPSC in this vehicle control (0.1% DMSO) rod/HC pair recovered by ∼40% after a 500-ms interval. **(B)** HC EPSCs from a different rod/HC pair after introducing dynasore (80 µM) into the presynaptic rod through a patch pipette. After introducing dynasore into the rod, the fast EPSC component (arrow) showed less recovery after 0.5 s than in the control response illustrated in A. **(C)** The fast EPSC component recorded from a voltage-clamped HC also showed little recovery with an interpulse interval of 0.5 s after dyngo-4A (30 µM) was introduced into a rod through a patch pipette. **(D)** Similar to the other inhibitors, the fast HC EPSC showed little recovery with an interpulse interval of 0.5 s after DIP (1 mM) was introduced into a rod through a patch pipette.

interpulse intervals. Changes in Q_{Ca} were similar in both control and test conditions (Fig. 4 D). The absence of any significant effects of dynasore, dyngo-4A, or DIP on paired pulse measurements of I_{Ca} indicates that effects on paired pulse recovery of EPSCs were not secondary to changes in Ca^{2+} influx (Babai et al., 2010; Van Hook et al., 2014).
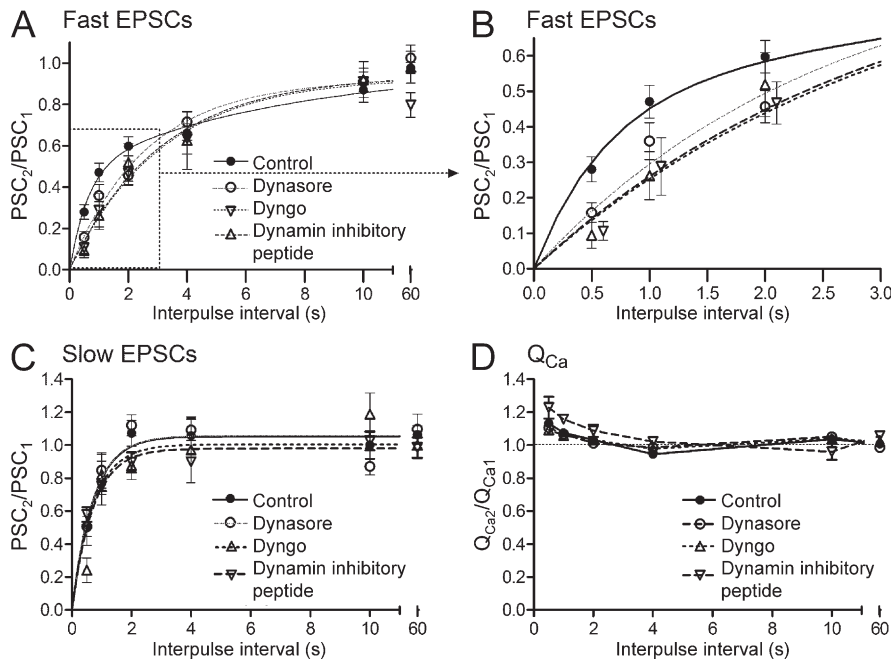
Figure 4. **Recovery from paired pulse depression of fast HC EPSCs was slowed by inhibiting endocytosis with dynasore, dyngo-4A, or DIP.** **(A)** Recovery from paired pulse depression of the fast EPSC component plotted as a function of interpulse interval (control, $n = 11$ pairs; dynasore [80 µM], $n = 15$ pairs; dyngo-4A [30 µM], $n = 10$; DIP [1 mM], $n = 7$). The amplitude of the second EPSC was normalized to the first EPSC in each pair. Recovery of the fast EPSC component was fit with a double exponential function. **(B)** The recovery observed with shorter interpulse intervals is replotted with the data points for dyngo-4A offset by 0.1 s from the others for ease of comparison. In control conditions, the fast time constant for recovery from paired pulse depression averaged 618 ms (solid lines and filled circles), slowing to 2.52, 3.24, or 3.06 s, respectively, in recordings where dynasore (dashed lines and open circles), dyngo-4A (dotted lines and downward triangles), or DIP (long dashes and upward triangles) were included in the rod patch pipette solution. The fast time constants obtained with dyngo-4A (P < 0.001, F test) and DIP (P = 0.0003, F test) were significantly slower than control. **(C)** Recovery from paired pulse depression of slow EPSC components was fit with a single exponential function. Time constants did not differ significantly among the four conditions (control, 732 ms; dynasore, 635 ms; dyngo-4A, 1,056 ms; DIP, 584 ms; P = 0.25, F test). **(D)** Paired pulse responses of I_{Ca} charge transfer (Q_{Ca}) showed a slight enhancement with short intervals and no paired pulse depression. Paired pulse responses of Q_{Ca} also did not differ among the four conditions. Error bars represent ±SEM.

Mobility of active zone Ca²⁺ channels increased when endocytosis was inhibited

We assessed the impact of inhibiting endocytosis with dynasore on the structure of the active zone by imaging movements of individual L-type Ca^{2+} channels at ribbon synapses in living rods. L-type Ca^{2+} channels lie in clusters beneath ribbons (Nachman-Clewner et al., 1999; Lv et al., 2012), where they move within small, confined membrane domains (Mercer et al., 2011). Channels were labeled by applying a primary antibody targeting the extracellular domain of the $\alpha_2\delta_4$ Ca^{2+} channel subunit and then tagging bound primary antibodies with QD-conjugated secondary antibodies. The confined movements of Ca^{2+} channels at rod synapses are illustrated by trajectory maps plotting the positions of individual QD-tagged Ca^{2+} channels mapped over time (Fig. 5 A). Channel confinement areas were quantified from the MSD of channels plotted against measurement time interval (Fig. 5, B–D). For diffusion within a confined domain, the MSD rises to a plateau of $L^2/3$, where L^2 is the membrane area in which channel movements are confined (Kusumi et al., 1993; Bannai et al., 2006).

We first measured movements of Ca^{2+} channels in the OPL of retinal slices where photoreceptor terminals are located. As shown in Fig. 5 B, confinement areas for Ca^{2+} channels in the OPL were enlarged significantly by treating slices with dynasore (80 µM; $L = 0.385 \pm 0.00579$ µm; $n = 11$) compared with control ($L = 0.227 \pm 0.00178$ µm; $n = 18$; P < 0.0001, F test). Confinement

areas were also enlarged significantly by treating slices with a membrane-permeant, myristoylated DIP (Fig. 5 B; Myr-QVPSRP NRAP-NH₂, 0.75 mM, Tocris; $L = 0.329 \pm 0.00333$ µm; $n = 12$) compared with a myristoylated control peptide (Myr-QPPASN PRVR-NH₂, 0.75 mM, $L = 0.236 \pm 0.00339$ µm; $n = 12$; P < 0.0001, F test). Treating slices with 20 mM KCl to stimulate vesicle cycling slightly increased confinement areas in control slices (Fig. 5 C; $L = 0.28 \pm 0.0042$ µm; $n = 10$; P < 0.0001, F test). Coapplication of dynasore with 20 mM KCl caused a further significant increase in confinement areas, nearly doubling the confinement length, L, to 0.50 ± 0.0046 µm ($n = 15$; P < 0.0001, F test).

In retinal slices, it can be difficult to determine whether a particular QD is attached to a rod or cone terminal. We therefore also examined enzymatically isolated individual rods (Fig. 5 D). In control conditions, L values averaged 0.20 ± 0.009 µm ($n = 15$) in Ca^{2+} channels of isolated rods. We found almost the same value for L in the presence of 20 mM KCl (0.199 ± 0.0012 µm; $n = 16$). Coapplication of dynasore with 20 mM KCl significantly expanded confinement areas, increasing L to 0.266 ± 0.0027 µm (Fig. 5 D; $n = 12$; P < 0.0001, F test). The finding that Ca^{2+} channel movements are less tightly constrained after treatment with dynasore shows that the active zone at rod ribbon synapses becomes more disorganized in the absence of compensatory endocytosis.

As with paired pulse experiments, the finding that Ca^{2+} channel confinement areas were expanded by both a small
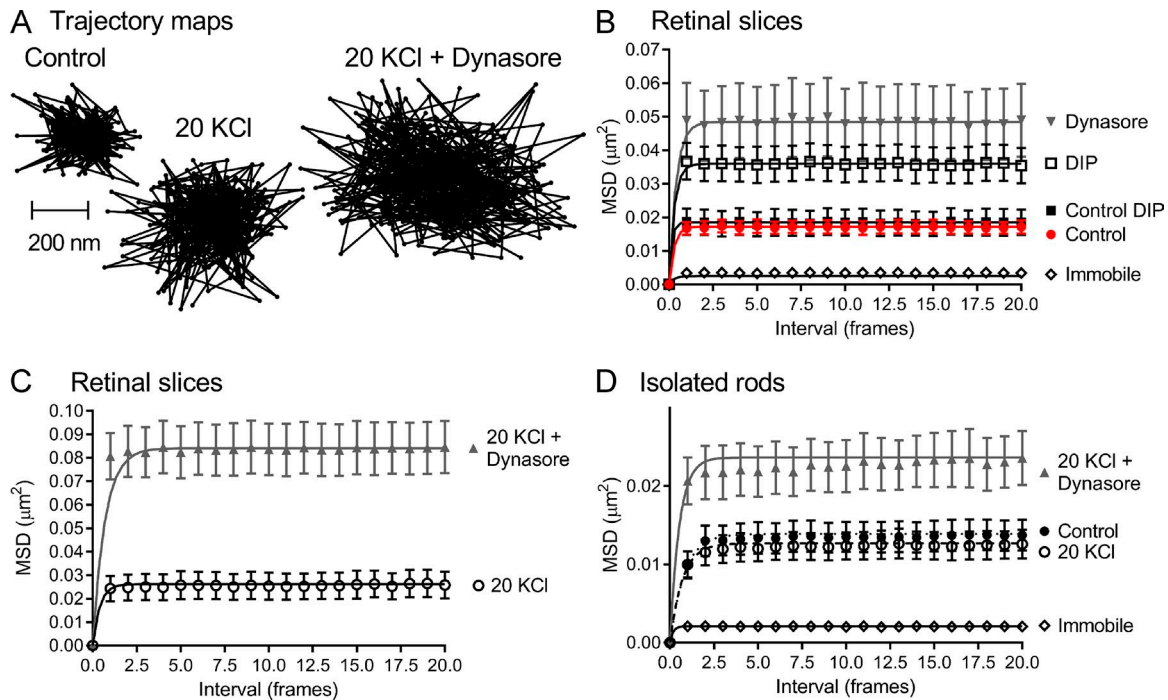
Figure 5. **Inhibition of endocytosis with dynasore (80 µM) increased lateral membrane mobility of Ca²⁺ channels. (A)** Trajectory maps illustrating the positions of individual Ca²⁺ channels labeled in the OPL with a primary antibody to the $\alpha_2\delta_4$ subunit and then tagged with a QD-conjugated secondary antibody. Channel positions were mapped every 30 ms for 12 s. Trajectory maps show the typical MSD observed in channels under control conditions during treatment with 20 mM KCl and with 20 mM KCl applied in the presence of dynasore. **(B)** MSD plotted as a function of measurement interval (30 ms/frame) for QDs in the OPL of retinal slices. The MSD was fit with a saturating curve as described in Materials and methods, attaining a plateau of $L^2/3$ where L^2 is the membrane area in which channel movements are confined. With the 1.2 NA, 60× objective, QDs immobilized in vacuum grease yielded $L = 0.087 \pm 0.00133$ µm ($n = 16$). Under control conditions, Ca²⁺ channels labeled with QDs yielded $L = 0.227 \pm 0.00178$ µm ($n = 18$). A similar value was obtained in the presence of a control version of a myristoylated DIP (Myr-QPPASNPRVR-NH₂, 0.75 mM, $L = 0.236 \pm 0.00339$ µm; $n = 12$). In the presence of dynasore (80 µM), L increased significantly (P < 0.0001, F test) to $L = 0.385 \pm 0.00579$ µm ($n = 11$). L also increased significantly relative to the control peptide with application of a myristolated DIP (Myr-QVP SRPNRAP-NH₂, 0.75 mM, Tocris; $L = 0.329 \pm 0.00333$ µm; $n = 12$; P < 0.0001, F test). **(C)** Application of 20 mM KCl alone yielded $L = 0.28 \pm 0.0042$ µm ($n = 10$). Coapplication of KCl with dynasore significantly increased L to 0.50 ± 0.0046 µm ($n = 15$; P < 0.0001, F test). **(D)** QDs measured in isolated rods using a 1.45 NA, 60× objective. In Ca²⁺ channels of isolated rods, L averaged 0.20 ± 0.009 µm ($n = 15$) under control conditions. In the presence of 20 mM KCl, $L = 0.199 \pm 0.0012$ µm ($n = 16$). Application of dynasore in the presence of 20 mM KCl significantly increased L to 0.266 ± 0.0027 µm ($n = 12$; P < 0.0001, F test). With immobilized QDs using a 1.45 NA, 60× objective, $L = 0.079 \pm 0.00129$ ($n = 10$). Error bars represent ±SEM.

molecule inhibitor, dynasore, and DIP suggests that this expansion was caused by inhibition of dynamin-mediated endocytosis and not by the dynamin-independent effects of dynasore. The synaptic location of Ca²⁺ channels implicates synaptic vesicle endocytosis, but does not rule out other forms of endocytosis. Inhibition of endocytic membrane turnover can alter membrane cholesterol levels (Preta et al., 2015), and depletion of membrane cholesterol increases Ca²⁺ channel mobility in salamander photoreceptors (Mercer et al., 2011). To examine potential changes in membrane cholesterol, we labeled cholesterol-rich lipid rafts with FITC-conjugated cholera toxin B (Mercer et al., 2011). In contrast to the depletion observed after treatment with cholesterol oxidase or methyl-β-cyclodextrin (Mercer et al., 2011), we found that application of dynasore (80 µM) for 10 min did not appreciably diminish labeling of the OPL in retinal slices by FITC-conjugated cholera toxin B ($n = 3$) compared with control slices prepared from the same retinas ($n = 3$). The finding that dynasore does not reduce membrane cholesterol in the OPL suggests that changes in Ca²⁺ channel mobility are not likely to be secondary to changes in cholesterol levels.

TIRFM imaging of single vesicles

The finding that inhibition of endocytosis slowed recovery of fast, ribbon-mediated responses from paired pulse depression suggests that it slowed the rate of vesicle replenishment at ribbon release sites. Slower replenishment can be caused by deficits in delivery of vesicles to the membrane, in docking, in priming, or in fusion. To distinguish various steps in the vesicle cycle, we examined the behavior of individual fluorescently labeled vesicles using TIRFM. We loaded synaptic vesicles in rod terminals with the fluid phase indicators Alexa Fluor 488 conjugated to either 3-kD or 10-kD dextran (Chen et al., 2013; Wen et al., 2017). We loaded retinas in darkness to maintain rods in a depolarized state and thereby promote vesicle turnover. We incubated retinas with dye for only a few minutes to limit dye loading to a small percentage of vesicles and thus ensure that fluorescent spots in synaptic terminals were likely to be individual vesicles rather than clusters of vesicles (Chen et al., 2013). Dye-loaded rods were dissociated and plated on coverslips for TIRFM imaging. Where the cell membrane contacts the glass, evanescent illumination creates a faint fluorescent footprint in which one can see individual dye-loaded vesicles at or near the membrane.
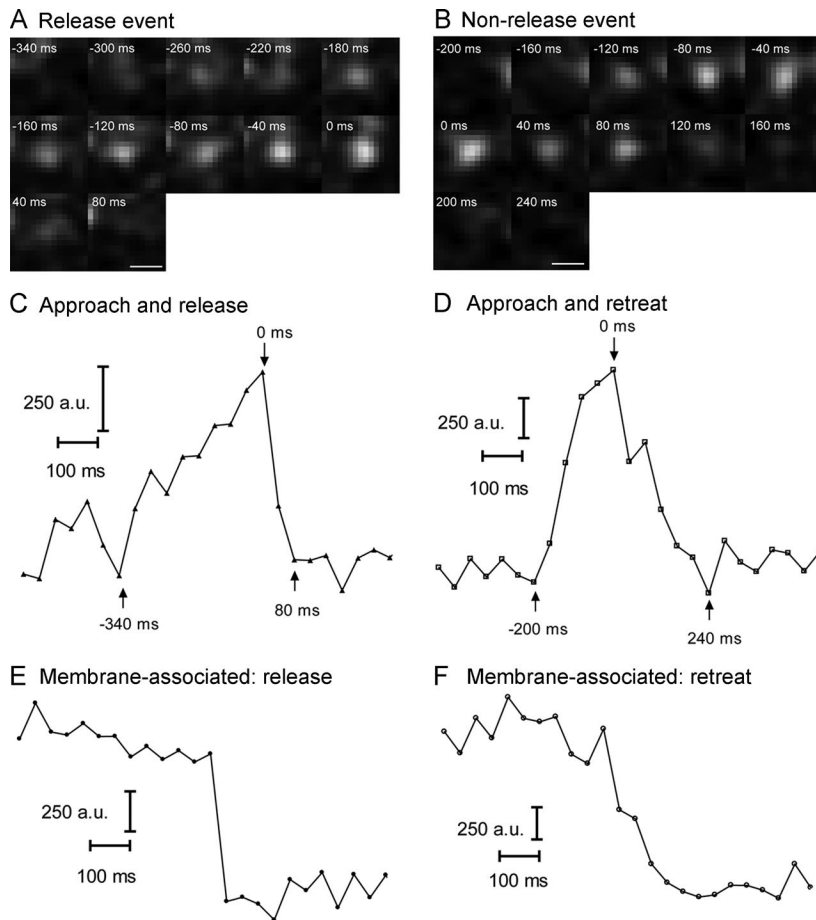
Figure 6. **Behavior of individual vesicles visualized using TIRFM. (A)** Sequence of images (40 ms/frame) showing a single vesicle loaded with 10-kD Alexa Fluor 488 as it approached the membrane and then fused. **(B)** Image sequence showing a vesicle that approached the membrane and then departed without fusion. Bars, 0.5 µm. **(C)** Changes in fluorescent brightness as a function of time plotted for a 7 × 7–pixel region of interest centered on the vesicle in A. Brightness increased as the vesicle approached the membrane and then declined abruptly after dye was released by fusion. Graph plots the fluorescence changes in arbitrary units (a.u.) measured at –340 to 80 ms (arrows). **(D)** Changes in fluorescent brightness as a function of time for the vesicle in B. As the vesicle retreated from the membrane, its brightness declined at roughly the same rate as it increased during membrane approach. Graph plots the fluorescence changes measured at –200 to 240 ms (arrows). **(E)** Fluorescence changes as a function of time from a vesicle that was stably associated with the membrane and then fused, causing its fluorescence to decline abruptly. **(F)** Fluorescence changes from a vesicle that was stably associated with the membrane but then departed without fusion, showing a gradual decline in fluorescence. These examples are all from rods loaded with 10-kD Alexa Fluor 488.

With TIRFM, fluorescence of a vesicle rises as it approaches the membrane, advancing through the exponentially increasing evanescent field of illumination at the interface between the membrane and the coverslip (Fig. 6, A–D). This is illustrated by the examples in Fig. 6 (A and B), which show image sequences (40 ms/frame) for single vesicles. Fluorescence changes measured within 7 × 7–pixel regions of interest are plotted as a function of time in Fig. 6 (C and D). After reaching the membrane and attaining maximal brightness, there are three possible fates for a vesicle: remain at the membrane surface, retreat from the membrane without fusion, or fuse with the plasma membrane. After fusion and release of intravesicular dye, vesicle fluorescence should decline abruptly, as illustrated by the image sequence in Fig. 6 A and the associated graph in Fig. 6 C. However, if a vesicle retreats from the membrane without fusion, its fluorescence should decline at roughly the same rate as it increased during membrane approach. This is illustrated by the example images in Fig. 6 B and graph in Fig. 6 D. Finally, vesicles can also remain stably associated with the membrane for many seconds. Vesicles in salamander rods average 45 nm in diameter (Thoreson et al., 2004), and so the evanescent field with a length constant of 65 nm (Chen et al., 2013) extends only about two vesicle diameters into the cell. In some ultrastructural studies, vesicles lying within two diameters of the membrane are defined as being docked (Verhage and Sørensen, 2008). Many of the membrane-associated vesicles visible by TIRFM ultimately went on to fuse with the plasma membrane and therefore also met functional criteria for

being docked. Fig. 6 E shows an example of a vesicle that was stably associated with the membrane at the beginning of a trial and then fused, causing its fluorescence to decline abruptly. Other membrane-associated vesicles retreated from the membrane without fusion, marked by a more gradual decline in fluorescence (Fig. 6 F). These data suggest that not all membrane-associated vesicles complete the docking process, but for the sake of brevity, we sometimes refer to membrane-associated vesicles as being "docked" in the text below.

To be defined as a release event, we required that vesicle fluorescence decline by at least 60% from peak fluorescence in the first frame of the decline phase and fall to baseline levels by the second frame (Chen et al., 2013; Wen et al., 2017). Fig. 7 A shows a sequence of images averaged from 16 fusion events that met those criteria. The fluorescence intensity measured in a 7 × 7–pixel region centered on the average vesicle is plotted in Fig. 7 C and shows a rapid decline in intensity after fusion. Consistent with earlier results from rods using this technique (Chen et al., 2013; Wen et al., 2017), average nonrelease retreat events ($n = 20$) showed a slower decline in fluorescence (Fig. 7, B and C) than fusion events. If dye particles are free to diffuse, then they should exit the small measurement region within ~1 ms (Wen et al., 2017). However, faint fluorescence persisted in the central region of the average fusion image for 160 ms after fusion (Fig. 7 C). This may reflect persistence of sticky, dextran-conjugated dye molecules in the restricted submembrane space beneath the release site. Residual fluorescence might also involve contributions
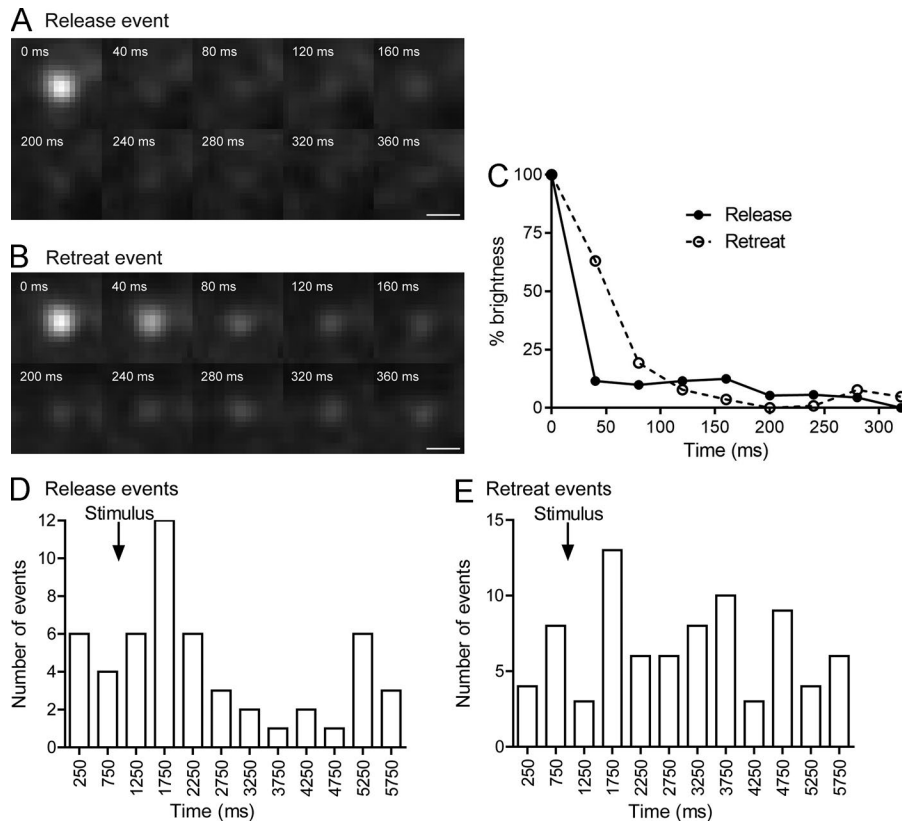
A Release event

| 0 ms | 40 ms | 80 ms | 120 ms | 160 ms |
| 200 ms | 240 ms | 280 ms | 320 ms | 360 ms |

B Retreat event

| 0 ms | 40 ms | 80 ms | 120 ms | 160 ms |
| 200 ms | 240 ms | 280 ms | 320 ms | 360 ms |

C

D Release events

E Retreat events

Figure 7. **Average vesicle behavior visualized by TIRFM. (A)** Sequence of images (40 ms/frame) showing release events averaged from 16 vesicles. **(B)** Sequence of images (40 ms/frame) showing nonrelease retreat events averaged from 20 vesicles. Bars, 0.5 µm. **(C)** Changes in fluorescent brightness as a function of time measured within a 7 × 7–pixel region of interest centered on the average vesicle images shown in A and B. Brightness declined much more rapidly after fusion than when vesicles retreated from the membrane without fusion. **(D)** Histogram plotting the number of release events before and after application of a depolarizing step (–70 to –10 mV, 100 ms applied at 1 s) to voltage-clamped rods (52 events in 7 rods). **(E)** Histogram plotting the number of nonrelease retreat events before and after application of a depolarizing step (–70 to –10 mV, 100 ms) to voltage-clamped rods (80 events in 7 rods). For experiments in this figure, rods were loaded with 3-kD Alexa Fluor 488.

from vesicles resting farther away from the membrane (e.g., up the ribbon) at the edge of the evanescent field. The average image of vesicles that retreated from the membrane without release showed a slightly more pronounced residual central fluorescence, suggesting the presence of a vesicle lingering at the edge of the evanescent field (Fig. 7 B). This fluorescence might come from a vesicle that did not fully exit the evanescent field after retreating from the membrane, or it might come from an entirely different vesicle sitting farther up the ribbon. Similar to results observed for vesicles loaded with 10-kD pHrodo (Chen et al., 2013), fusion events defined by these criteria for vesicles loaded with 3-kD Alexa Fluor 488 were increased by stimulation with depolarizing steps (–70 to –10 mV, 100 ms) applied to voltage-clamped, isolated rods (Fig. 7 D). Vesicles that disappeared more slowly and did not fulfill these criteria were defined as nonrelease retreat events. The frequency of nonrelease events did not appear to be increased by depolarizing stimulation (Fig. 7 E).

We compared vesicle behavior in rods during bath application of dynasore or vehicle control (0.1% DMSO) solution. We first examined the origins and fates of synaptic vesicles during 6-s trials with vesicles loaded with either 3-kD Alexa Fluor 488 (Fig. 8 A) or 10-kD Alexa Fluor 488 (Fig. 8 B). In this experiment, synaptic release was stimulated by depolarizing rod terminals with a 2-s puff of 50 mM KCl. Because rods were loaded with dye before treatment with dynasore, we expected that slowing vesicle turnover by inhibiting endocytosis should promote the retention of dye-loaded vesicles. However, rather than seeing more vesicles, we saw fewer vesicles advance toward the membrane in rods treated with dynasore compared with control conditions (Fig. 8, A and B), suggesting that vesicle delivery to the membrane was

impaired by inhibiting endocytosis (3 kD, P < 0.0001; 10 kD, P < 0.0001; unpaired *t* tests). The speed at which vesicles approached the membrane was unchanged by dynasore, suggesting that this was not caused by a general loss of vesicle mobility. We calculated vesicle velocity from the distance traveled by a vesicle between the final two frames (40 ms apart) as it approached the membrane. We converted the increase in fluorescence to distance using the length constant for TIRFM illumination measured with the 488-nm laser of ∼57 nm (Chen et al., 2013; Wen et al., 2017). In control conditions, final approach velocity averaged 1,004 ± 19 nm/s (*n* = 25). We obtained a similar mean velocity in cells treated with dynasore (895 ± 14 nm/s, *n* = 23; P = 0.648).

Although fewer vesicles advanced toward the membrane, the number of membrane-associated vesicles detected at the beginning of each trial did not differ significantly between dynasore and control cells (Fig. 8, A and B). The number of vesicles that remained at the membrane surface at the end of each trial was also unchanged by dynasore treatment when we examined vesicles loaded with 3-kD Alexa Fluor 488 and was increased slightly for vesicles loaded with 10-kD Alexa Fluor 488 (P = 0.043, unpaired *t* test). These results show that although fewer vesicles approached the membrane in dynasore-treated rods, the ability of vesicles that reached the membrane to initiate early steps in the docking process was not significantly impaired by inhibition of endocytosis.

Dynasore treatment significantly reduced the frequency of vesicles that fused during depolarizing stimulation with a puff of 50 mM KCl (Fig. 8, A and B). The frequency of vesicles that departed the membrane without fusion was also significantly reduced (Fig. 8, A and B). Vesicles typically fused soon after
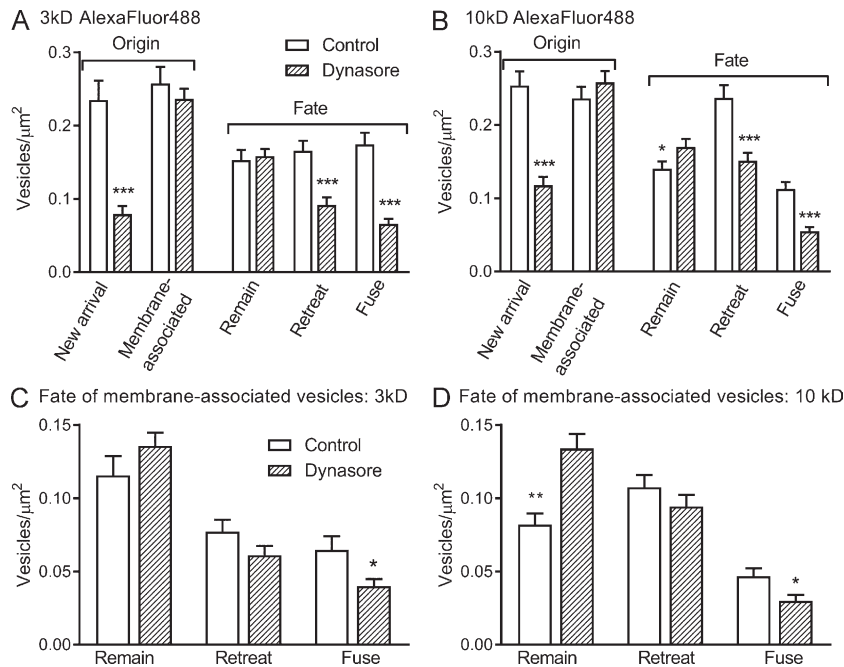
A 3kD AlexaFluor488

Origin

□ Control
▨ Dynasore

Fate

Vesicles/μm² (y-axis: 0.0, 0.1, 0.2, 0.3)

New arrival, Membrane-associated, Remain, Retreat, Fuse

B 10kD AlexaFluor488

Origin

Fate

Vesicles/μm² (y-axis: 0.0, 0.1, 0.2, 0.3)

New arrival, Membrane-associated, Remain, Retreat, Fuse

C Fate of membrane-associated vesicles: 3kD

□ Control
▨ Dynasore

Vesicles/μm² (y-axis: 0.00, 0.05, 0.10, 0.15)

Remain, Retreat, Fuse

D Fate of membrane-associated vesicles: 10 kD

Vesicles/μm² (y-axis: 0.00, 0.05, 0.10, 0.15)

Remain, Retreat, Fuse

Figure 8. **Comparing the origins and fates of vesicles in the presence and absence of dynasore. (A and B)** Vesicle behavior in vehicle control (0.1% DMSO) or dynasore (80 μM) during 6-s trials. Vesicles were loaded with either 3-kD Alexa Fluor 488 (A) or 10-kD Alexa Fluor 488 (B). Synaptic release was stimulated by depolarizing rod terminals with a 2-s puff of 50 mM KCl. With both dyes, significantly more vesicles advanced toward the membrane in vehicle control solutions than in rods treated with dynasore (3 kD, $P < 0.0001$; 10 kD, $P < 0.0001$; unpaired t tests). The number of vesicles that began each trial stably associated with the membrane did not differ significantly between dynasore and control cells. The number of vesicles that remained at the membrane surface at the end of each trial was not altered significantly by dynasore treatment with 3 kD–loaded vesicles but was increased slightly with 10-kD vesicles ($P = 0.043$). Dynasore treatment significantly reduced the frequency of vesicles that fused during depolarizing stimulation with a puff of 50 mM KCl (3 kD, $P < 0.0001$; 10 kD, $P < 0.0001$). The number of vesicles that departed the membrane without fusion was also significantly reduced (3 kD, $P < 0.0001$; 10 kD, $P < 0.0001$). **(C and D)** In the subset of vesicles loaded with 3-kD Alexa Fluor 488 (C) or 10-kD Alexa Fluor 488 (D) that began each trial as membrane-associated vesicles, we found no significant difference in the number of nonrelease retreat events (3 kD, $P = 0.12$; 10 kD, $P = 0.25$), but dynasore significantly decreased fusion (3 kD, $P = 0.014$; 10 kD, $P = 0.012$). The number of vesicles loaded with 10-kD Alexa Fluor 488 that remained at the membrane throughout the entire trial was also increased significantly by dynasore ($P < 0.0001$). Error bars represent ±SEM. *, $P < 0.05$; **, $P < 0.001$; ***, $P < 0.0001$.

reaching the membrane, akin to "crash fusion" observed in neuroendocrine cells (Verhage and Sørensen, 2008). One contributor to a reduction in the numbers of departure and fusion events was simply that fewer vesicles approached the membrane after dynasore treatment. To control for this, we examined the fate of vesicles that began the trial as membrane-associated vesicles (Fig. 8, C and D). In this subset, we found no significant difference in the number of nonrelease retreat events with dynasore treatment (3 kD, $P = 0.12$; 10 kD, $P = 0.25$; unpaired t tests), suggesting that the reduction in retreat events (Fig. 8, A and B) was simply a consequence of a reduction in the number of vesicle approach events. However, dynasore significantly decreased fusion among membrane-associated vesicles (3 kD, $P = 0.014$; 10 kD, $P = 0.012$; unpaired t tests), indicating that in addition to a reduction in the number of approaching vesicles, vesicle fusion was directly impaired by inhibition of endocytosis.

The number of vesicles loaded with 3-kD Alexa Fluor 488 that began and ended trials as membrane-associated vesicles was not affected by dynasore (Fig. 8 C). However, there was a significant increase in the number of vesicles loaded with the larger dye, 10-kD Alexa Fluor 488, which remained at the membrane throughout each trial (Fig. 8 D; $P < 0.001$, unpaired t test). Increased persistence of 10-kD Alexa Fluor 488–loaded vesicles at the membrane with dynasore treatment was also evident from the analysis shown in Fig. 8 B. This increased persistence of membrane-associated vesicles loaded with 10-kD dye is consistent with recent findings from our laboratory that 10-kD dyes

are retained more frequently in vesicles after fusion than 3-kD dyes. These results were interpreted as being caused by contributions from kiss-and-run fusion that releases small dyes more efficiently than larger dyes (Wen et al., 2017). The retention of more membrane-associated vesicles loaded with larger 10-kD dyes may reflect vesicles that failed to release large dye molecules during kiss-and-run fusion and were subsequently trapped at the membrane when endocytic fission was blocked by dynasore (Logiudice et al., 2009).

Impact of dynasore on ribbon-mediated release visualized by TIRFM

Electrophysiological experiments suggested that ribbon-mediated release is more sensitive to inhibition of endocytosis than nonribbon release. To compare the behavior of vesicles near and far from ribbons, we loaded retinas with 3-kD dextran-conjugated Alexa Fluor 488 and then performed whole-cell patch-clamp recordings in dissociated rods. We labeled the ribbons in these rods by introducing a tetramethylrhodamine-conjugated, Ribeye-binding peptide through the patch pipette. We examined the behavior of individual vesicles evoked by a depolarizing step (–70 to –10 mV, 100 ms) in the presence or absence of 80 μM dynasore. Fig. 9 shows fluorescent images of synaptic terminals from control and dynasore-treated rods visualized by TIR FM. The left panels show average fluorescence images of control (Fig. 9 A) and dynasore-treated (Fig. 9 B) rod terminals in which vesicles were loaded with 3-kD Alexa Fluor 488 (mean of 150
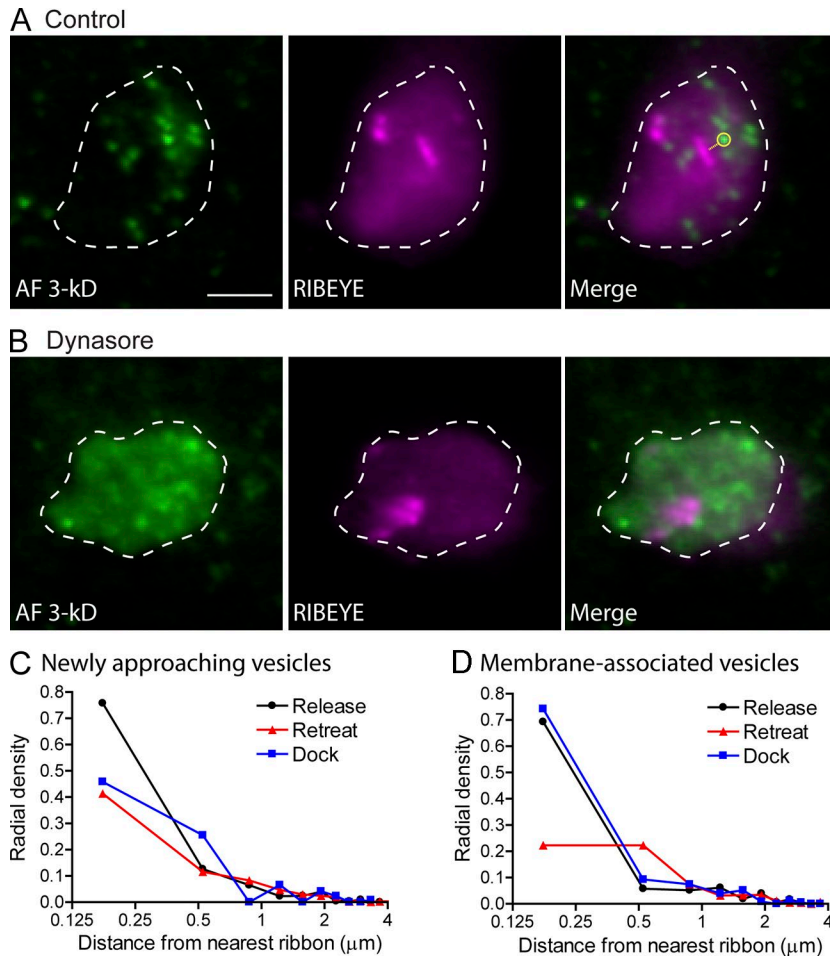
Wen et al.
Endocytosis restores release at ribbon synapses

Journal of General Physiology 603
https://doi.org/10.1085/jgp.201711919

Figure 9. **Visualization of vesicles and ribbons by TIR FM in rod terminals.** The figure shows the synaptic terminals of rods in which vesicles were loaded with 3-kD Alexa Fluor 488 and ribbons were labeled by introducing a Ribeye-binding peptide conjugated to tetramethylrhodamine through the patch pipette. **(A)** Terminal of an isolated rod in control conditions (0.1% DMSO). **(B)** Rod terminal in the presence of dynasore (80 µM). The green fluorescence images at the left of A and B show vesicles loaded with 3-kD Alexa Fluor 488 after averaging the entire trial (150 frames, 40 ms apiece). Differences in vesicle brightness in these average images were largely caused by differences in the amount of time that a vesicle spent near the membrane during the acquisition period rather than intrinsic differences in vesicle brightness. The magenta images in the middle show the location of ribbons labeled by tetramethylrhodamine-conjugated Ribeye-binding peptide. The 561-nm laser was tilted to deepen penetration of the evanescent field into the cell and illuminate tetramethylrhodamine-labeled ribbons more effectively. As illustrated in the merged image at the right of A, we measured the distance between the center of a vesicle to the edge of the nearest ribbon. Bar, 5 µm. **(C)** Fates of newly approaching vesicles in control conditions. The relative frequency histogram of vesicle events as a function of distance from the nearest ribbon was binned at 350-nm intervals and adjusted for radial density (see Materials and methods). The likelihood of observing a newly approaching vesicle was consistently greater in the bin closest to the ribbon. However, the probability that fusion of a newly approaching vesicle (n = 48 total events in 9 rods) would occur in the bin closest to the ribbon rather than farther away was significantly greater than the probability that a newly approaching vesicle would dock at the membrane close to the ribbon (n = 17; P = 0.023, z test) or depart from ribbon-proximal membrane without fusion (n = 157; P < 0.0001, z test). **(D)** Fates of vesicles that began a trial as membrane-associated or docked vesicles. Fusion of previously docked vesicles was significantly more likely to occur in the bin closest to the ribbon (n = 30 total events; P = 0.00014) than retreat from the membrane (n = 35). The likelihood that a vesicle would remain docked throughout the trial was also significantly more likely in the bin closest to the ribbon (n = 28; P < 0.0001) than retreat.

frames, 40 ms apiece). Brightness differences among vesicles in these average images were largely caused by differences in the amount of time that vesicles spent near the membrane during the acquisition period.

Differences between control (0.1% DMSO) and dynasore-treated (80 µM) rods in the total number of events in voltage-clamp experiments were consistent with the high K+ stimulation experiments described above (Fig. 8). Half as many vesicles approached the membrane in dynasore-treated rods (106 vesicles; rods, n = 8) than in control rods (222 vesicles; rods, n = 9). And although vesicle advance was diminished in dynasore, the number of membrane-associated vesicles at the beginning (control, n = 93; dynasore, n = 84) and end (control, n = 45; dynasore, n = 38) of trials were similar in the two conditions. Finally, consistent with impaired fusion, the number of release events was reduced from 78 in control rods to 38 in dynasore-treated rods. Retreat events were also reduced from 192 in control to 106 in dynasore.

After acquiring two to three stimulation trials per cell, we imaged tetramethylrhodamine-labeled ribbons using 561-nm laser excitation. Rod ribbons sit above the plasma membrane atop an arciform density and can extend up to a micron into the cell. We angled the laser to deepen penetration of the evanescent field and illuminate the ribbons more effectively. The magenta images in the middle of Fig. 9 show ribbons labeled by the tetramethylrhodamine-conjugated Ribeye-binding peptide in both the control (Fig. 9 A) and dynasore-treated (Fig. 9 B) rod terminals. Merged vesicle and ribbon images are shown in the right panels (Fig. 9, A and B).

We measured the distance from the center of each vesicle to the edge of the nearest ribbon. We measured the relative frequency of events using a distance-from-ribbon bin size of 350 nm, matching the optical point spread function measured with this objective (Chen et al., 2013). We adjusted the frequency of events by the annular area occupied by each radial bin to calculate the radial density of events (see Materials and methods).

Wen et al.
Endocytosis restores release at ribbon synapses

In control conditions (0.1% DMSO), the likelihood that a newly arriving vesicle would be released was greatest in the bin closest to the ribbon and dropped off sharply with increasing distance from the ribbon (Fig. 9 C). The likelihood that a newly arriving vesicle would retreat from the membrane or that it would remain as a membrane-associated vesicle was also greater near ribbons. However, membrane retreat and stable association with the membrane were both less likely to occur near ribbons than fusion (Fig. 9 C). For vesicles that began the trial as membrane-associated vesicles (Fig. 9 D), most either fused before the end of the trial or remained as membrane-associated vesicles throughout the trial. Few of the membrane-associated vesicles located close to ribbons retreated from the membrane without fusion (Fig. 9 D). This suggests that docked vesicles rarely retreat back up the ribbon and is consistent with a study from bipolar cells showing that vesicles almost always exit the ribbon at its base (Vaithianathan and Matthews, 2014). The clustering of vesicles near ribbons is consistent with the central role of ribbons in release. However, there are also upper limits on the possible distance between a vesicle and its nearest ribbon because of limits in terminal size (up to 5 µm diameter) and the presence of multiple ribbons in the same salamander rod terminal (Townes-Anderson et al., 1985; Van Hook and Thoreson, 2015).

When endocytosis was inhibited by dynasore, various aspects of vesicle behavior were changed. As discussed above, the total number of vesicles that approached the membrane was reduced by dynasore treatment (Fig. 8). The radial distribution of vesicles that approached the membrane and then retreated without fusion did not differ in control versus dynasore-treated cells, indicating that the likelihood of membrane approach was impaired equally at both ribbon and nonribbon sites (Fig. 10 A). However, the frequency of vesicles that fused soon after reaching the membrane was diminished significantly in the bin closest to the ribbon by dynasore treatment (Fig. 10 B). The frequency of vesicles that arrived near ribbons and then remained or docked at the membrane was increased in dynasore-treated rods (Fig. 10 C). Thus, unlike control rods where fusion was more common than docking at ribbons, vesicles arriving at ribbons in dynasore-treated rods rarely fused and more often docked. This suggests that vesicles that failed to fuse soon after arriving at the membrane in dynasore-treated rods were capable of initiating the docking process. For vesicles that began trials as membrane-associated or docked vesicles, dynasore caused them to be less likely to remain docked and more likely to retreat from the membrane (Fig. 10, D and E). Thus, although newly arriving vesicles can initiate docking at ribbons in dynasore-treated rods, inhibition of endocytosis appears to limit the ability of vesicles to progress to final stages of the release process. Although the overall likelihood of fusion was reduced by dynasore treatment, membrane-associated vesicles were still more likely to fuse at ribbons than at nonribbon locations (Fig. 10 F), consistent with a key role for the ribbon in facilitating release even after endocytosis was inhibited.

Discussion

In addition to its role in recycling vesicles, endocytosis is important for restoring release site function after prior release (Kawasaki et al., 2000; Hosoi et al., 2009; Neher, 2010; Hua et al., 2013; Lipstein et al., 2013; Mahapatra et al., 2016). At conventional synapses, this role for endocytosis is typically evident only at high stimulation frequencies of 100 Hz or greater (Lipstein et al., 2013), where it appears to set an upper limit on release rates (Neher, 2017). Our results show that the restoration of release site function by endocytosis is crucial for allowing continued release at photoreceptor ribbon synapses at much more modest frequencies. The greater sensitivity to endocytic restoration at photoreceptor ribbon synapses may derive from the fact that photoreceptor ribbons release multiple vesicles at the same active zone, whereas release at the calyx of Held occurs at hundreds of active zones, but with each active zone releasing only one or two vesicles at a time (Taschenberger et al., 2002). Inhibiting endocytosis significantly slowed recovery from paired pulse depression of fast, ribbon-related release from rods and inhibited the ability of second-order HCs to follow rod light responses at frequencies as low as 2 Hz. The ability of dynasore to rapidly inhibit ribbon-mediated, fast release from rods without any intervening stimulation suggests that even occasional spontaneous release events in rods (Maple et al., 1994; Cork et al., 2016) may be sufficient to impair subsequent release when endocytosis is inhibited.

Several different lines of evidence indicate that the impairment of fast, ribbon-mediated release that occurs in response to inhibition of endocytosis is caused by a reduced availability of functional ribbon release sites. First, the speed at which release was impaired during bath application of dynasore in the absence of any intervening stimulation cannot be readily explained by a depletion of the releasable pool of vesicles. After the initial decline in fast release during the first 2 min of dynasore treatment, fast release declined at the same rate as in control tissue, suggesting that dynasore did not significantly deplete the ribbon-associated pool over that time. The decline in fast release was also not paralleled by changes in slow release, which proceeded more gradually, or by changes in spontaneous release, which did not decline at all during 8-min bath application of dynasore. Although it is possible that different pools of vesicles may participate in different modes of release (Crawford and Kavalali, 2015), blocking vesicle refilling in rods with bafilomycin caused spontaneous release to decline more rapidly, not more slowly, than evoked release (Cork et al., 2016). Further evidence for impaired replenishment of ribbon release sites came from the finding that inhibiting endocytosis with dynasore or dyngo-4A slowed the rate at which fast, ribbon-mediated release at rod synapses, but not slow release, recovered from paired pulse depression. The ability of dynasore treatment to increase Ca^{2+} channel mobility provided direct evidence for disorganization of release site structure after inhibition of endocytosis. Finally, TIRFM experiments showed that the fusion of vesicles at or near ribbons was directly impaired by dynasore treatment.

The relatively large size of rods in salamander retina allowed us to perform paired recordings, TIRFM, and single-particle
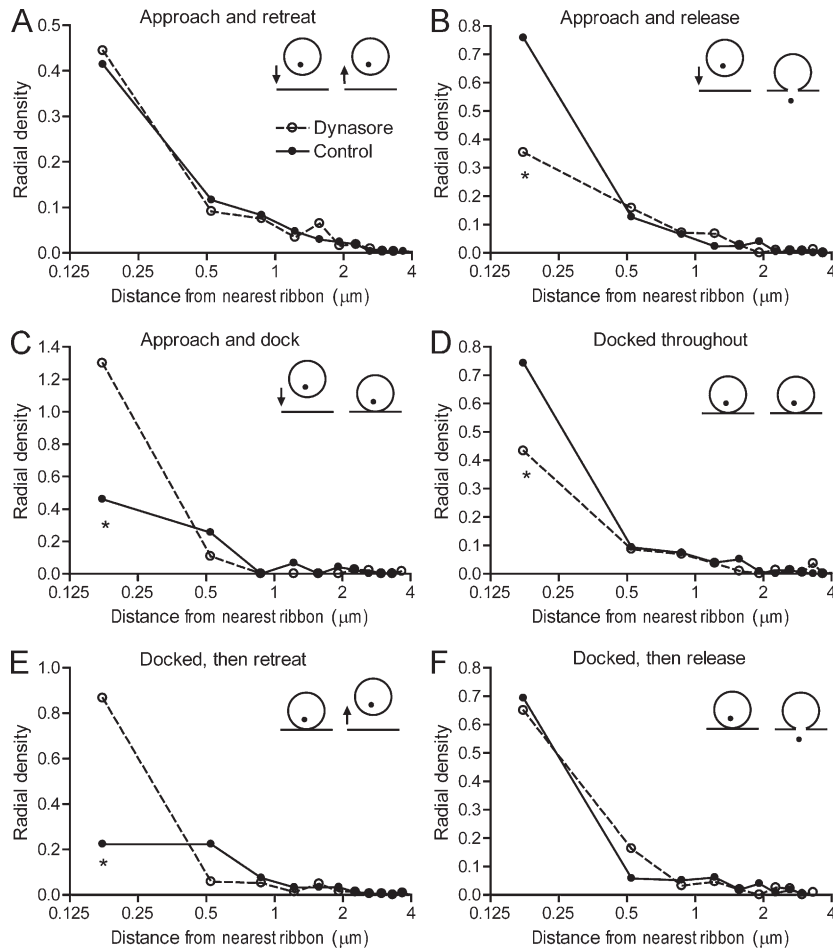
Wen et al.
Endocytosis restores release at ribbon synapses

Journal of General Physiology
https://doi.org/10.1085/jgp.201711919

605

Figure 10. **Comparisons of the radial density distributions of vesicle behaviors in control (0.1% DMSO) versus dynasore-treated (80 µM) rods.** As in Fig. 9, the relative frequency of vesicle events as a function of distance from the nearest ribbon was binned at 350-nm intervals and adjusted for radial density. **(A)** Spatial distribution of vesicles that approached the membrane and then retreated without fusion did not differ between control and dynasore-treated rods (control, n = 157 events from 8 rods; dynasore, n = 76 events from 9 rods). **(B)** Distribution of vesicles that approached the membrane and then fused during the trial. In dynasore-treated rods, there was a significant decline in fusion of vesicles in the bin closest to the ribbon (control, n = 48; dynasore, n = 22; P < 0.0001, z test). **(C)** In the bin closest to the ribbon, there was also a significant increase in the likelihood that a newly arriving vesicle would remain at the membrane for the remainder of the trial in dynasore-treated rods (control, n = 17; dynasore, n = 8; P < 0.0001). **(D)** However, among vesicles that were docked at the membrane at the beginning of the trial, fewer remained at the membrane in the bin closest to the ribbon for the entire 6-s trial in dynasore-treated rods (control, n = 28; dynasore, n = 30; P < 0.0001). **(E)** In the bin closest to the ribbon, a larger fraction of membrane-associated vesicles retreated from the membrane without fusion in dynasore-treated rods (control, n = 35; dynasore, n = 30; P < 0.0001). **(F)** The likelihood of release for membrane-associated vesicles was similarly high with both control and dynasore-treated rods (control, n = 30; dynasore, n = 16) in the bin closest to the ribbon.

tracking experiments that we could not perform using mouse rods, but use of salamander retina precluded the use of genetic models. For most of these experiments, we used the small molecule dynasore to inhibit synaptic endocytosis in rods. In paired pulse replenishment experiments, we introduced dynasore through a patch pipette to limit effects to the presynaptic rod. However, in addition to inhibiting endocytic retrieval of synaptic vesicles, dynasore can inhibit other forms of endocytosis and influence other aspects of cell behavior (Girard et al., 2011; Park et al., 2013; Preta et al., 2015). We therefore also tested effects on paired pulse depression of a more potent inhibitor, dyngo-4A, and DIP. It is unlikely that off-target effects of dynasore on dynamin-independent processes are shared with DIP. Thus, the finding that all three compounds caused a similar slowing of recovery from paired pulse depression argues that impaired vesicle replenishment was a consequence of impaired dynamin-mediated endocytosis and not of other effects of dynasore. We also found that both dynasore and a myristoylated form of DIP caused similar increases in Ca²⁺ channel mobility. Although dynasore can alter membrane cholesterol levels (Preta et al., 2015) and cholesterol depletion can increase Ca²⁺ channel mobility (Mercer et al., 2011), dynasore treatment did not produce observable changes in the density of cholesterol-rich lipid rafts in photoreceptor terminals stained with FITC-conjugated CTX$_B$. For TIRFM experiments, we only tested dynasore and cannot rule out the possibility that some of dynasore's effects might reflect actions on targets other than dynamin. However, collectively, our results suggest that the synaptic changes we observed were likely caused by effects of these inhibitors on dynamin-dependent, synaptic vesicle endocytosis.

Allowing Ca²⁺ channels to move farther away from release sites by increasing the size of Ca²⁺ channel confinement domains can weaken positional priming and reduce release efficiency (Mercer et al., 2012). The increases in Ca²⁺ channel mobility produced by dynasore or DIP may therefore reduce release efficiency. However, reducing release efficiency has a bigger impact on the kinetics of release than on the total amount of release because moving Ca²⁺ channels a bit farther away from release sites will generally just lengthen the time it takes for Ca²⁺ to rise to the levels needed for fusion at release sites. So although expansion of Ca²⁺ channel confinement domains provides direct evidence for change of release site structure, this expansion is probably not a major contributor to the overall reduction in synaptic release produced by dynamin inhibition.

Our results showed that ribbon-mediated release in rods recovered from paired pulse depression with a biexponential time course similar to that observed in cones (Van Hook et al., 2014; Thoreson et al., 2016). Under normal circumstances, the principal rate-limiting step that limits synaptic transmission to HCs during sinusoidal stimulation of cones is the fast component of this replenishment process that has a time constant of 600–800 ms (Innocenti and Heidelberger, 2008; Van Hook et al.,

2014; Grabner et al., 2016; Thoreson et al., 2016). In both rods and cones, this fast replenishment process involves actions of Ca^{2+} operating through calmodulin to enhance vesicle attachment to the ribbon and thereby speed replenishment of ribbon release sites (Van Hook et al., 2014; Van Hook and Thoreson, 2015). The present results indicate that although vesicles may be returned to ribbons by this process, newly delivered vesicles cannot be efficiently released from ribbons until endocytosis has restored release sites to fusion competence. Thus, when endocytosis is inhibited, the process of release site clearance becomes the rate-limiting step in replenishment, slowing the time constant for replenishment three- or fourfold to 2.5–3.2 s.

The need to quickly restore release site function may provide a rationale for the rapid rate of endocytosis observed at photoreceptor synapses with time constants of a few hundred milliseconds (Van Hook and Thoreson, 2012; Cork and Thoreson, 2014; Wen et al., 2017). Simply restoring the cytoplasmic vesicle pool would not necessitate such rapid retrieval because refilling of newly retrieved vesicles with glutamate is considerably slower with a time constant of ~15 s (Hori and Takahashi, 2012). Rapid endocytosis in photoreceptors appears to involve significant contributions from kiss-and-run release in which vesicles fuse transiently with the plasma membrane through a narrow fusion pore (Wen et al., 2017). The preferential retention of 10-kD Alexa Fluor 488 near the membrane in TIRFM experiments is consistent with the presence of kiss-and-run events that preferentially release small 3-kD dyes over 10-kD dyes. In addition to facilitating rapid retrieval, kiss-and-run may minimize changes to the surface area and contents of the plasma membrane that would be caused by insertion of vesicle lipids and proteins during full-collapse fusion.

Unlike fast ribbon-mediated release, slow release from rods involves significant contributions from nonribbon sites that can be triggered by CICR (Chen et al., 2013, 2014). The locations of nonribbon release events vary from trial to trial, suggesting that ectopic release sites are not fixed in location or, alternatively, that they are fixed but show extremely low release probability (Chen et al., 2014). With either scenario, prior release at a nonribbon site should have little impact on subsequent release. Consistent with this, treatment with dynasore did not rapidly impair slow release, nor was recovery of slow release from paired pulse depression significantly altered. TIRFM experiments also showed that dynasore treatment caused more significant changes in release at ribbon than nonribbon sites. Although slow release was not immediately affected by dynasore, it declined gradually with prolonged application. The gradual decline in slow release might involve depletion of a pool of vesicles involved in slow but not fast or spontaneous release. It might also involve obstructions created by the accumulation of hemifused vesicles in perisynaptic membrane that occurs during dynasore treatment (Logiudice et al., 2009). This might also account for the observation in TIRFM experiments that fewer vesicles advanced toward the membrane in dynasore-treated rods.

TIRFM experiments provided insights into the behavior of vesicles at ribbons and how that behavior was altered by inhibition of endocytosis. One possible concern is that some fusion events may have been mis-categorized as retreat events or vice versa. Such miscategorization would obscure the differences between release and retreat events observed under various experimental conditions. For example, consider Fig. 8 (C and D), in which dynasore caused a significant decline in the number of fusion events among membrane-associated vesicles. If some fusion events were not accurately identified, but were instead miscategorized as retreat events, then this might account for the small decline in retreat events that was seen in this same experiment (Fig. 8). And if so, this would also suggest that dynasore had even greater effects on the likelihood of fusion. Although some events may have been miscategorized, it is clear that our criteria were at least moderately successful in separating release and retreat events. If these criteria were completely incapable of distinguishing these events, then it would not be possible to distinguish any differences whatsoever in dynasore's effects on release versus retreat. Therefore, the data in Figs. 8 and 10 showing that dynasore had significantly different effects on release and retreat events support conclusions from other evidence (Chen et al., 2013; Wen et al., 2017) that release events can be reliably distinguished from retreat events.

In control rods, TIRFM results showed that most vesicles fused soon after arriving at the membrane near ribbons. The short period of time that vesicles generally spend at the membrane before fusion is consistent with the idea that vesicles are primed during descent down the ribbon and therefore are ready for almost immediate release (Snellman et al., 2011; Mehta et al., 2013). Fewer newly arriving vesicles docked at the membrane or retreated without fusion. For those vesicles that successfully docked, very few retreated from the membrane without fusing. These results are consistent with experiments from bipolar cells suggesting that vesicles almost always exit ribbons at their base and rarely return up the ribbon (Vaithianathan and Matthews, 2014).

Although the number of newly approaching vesicles was reduced in dynasore-treated rods, the number of membrane-associated or docked vesicles was not (Fig. 8). This suggests that vesicles that successfully reach the membrane can initiate early steps in docking. Unlike control rods where ribbon-associated vesicles often fused soon after reaching the membrane, vesicles located near ribbons in dynasore-treated rods were more likely to retreat soon after arrival or to dock at the membrane for a time and then retreat. These results suggest that, after inhibiting endocytosis, vesicles descending the ribbon are more likely to encounter nonfunctional release sites at the ribbon base and are therefore less likely to be released immediately after reaching the membrane, instead lingering near the membrane. Although some of these membrane-associated vesicles may ultimately fuse, others simply retreat from the membrane.

We initially hypothesized that perhaps the reduction in the number of vesicles that approach the membrane in dynasore-treated rods may occur because vesicle approach might be obstructed by an accumulation of unretrieved, hemifused vesicles resulting from the inhibition of vesicle fission by dynasore. However, endocytosis in photoreceptors is thought to occur primarily in perisynaptic regions (Wahl et al., 2013; Fuchs et al., 2014), and we did not see a greater impairment of vesicle approach at nonribbon sites compared with ribbon sites.

Furthermore, we examined electron micrographs of rod and cone terminals treated with dynasore and did not see an obvious accumulation of vesicles at the membrane surface (unpublished data). Instead, perhaps local changes in active zone structure caused by inhibition of endocytosis may propagate into the surrounding protein network and impede vesicle approach.

Our results show that rod ribbons are particularly sensitive to inhibition of endocytosis and subsequent disruption of release site function, limiting the ability of second-order HCs to follow rod light responses at quite modest frequencies. This sensitivity likely involves the structure of synaptic ribbons where many vesicles are clustered closely together along the base, separated from one another by as little as 10 nm (Lasansky, 1978; Thoreson et al., 2004). Similar to photoreceptors, bipolar cells are capable of a rapid form of endocytosis with time constants of 1–2 s that would support rapid restoration of release site function (von Gersdorff and Matthews, 1994). However, although endocytic restoration of release site competence may be important at retinal ribbon synapses, it does not appear to be as critical for sustained release at hair cell ribbon synapses. These synapses are capable of sustaining release of large numbers of synaptic vesicles during maintained depolarization (Graydon et al., 2011; Schnee et al., 2011) but use relatively slow forms of endocytosis (Parsons et al., 1994; Moser and Beutner, 2000). Cones can follow higher frequencies than rods, but fast endocytosis was not inhibited in cones as effectively by dynasore (Van Hook and Thoreson, 2012), and so we did not have the pharmacological tools to test the role of endocytosis in these cells.

Although ribbon-mediated fusion was disrupted, early steps in docking were not impaired by treatment with dynasore. This argues against the idea that prior vesicle release events impede subsequent fusion primarily by impairing vesicle docking (e.g., as a consequence of the accumulation of "used" vesicular proteins, such as cis-SNARE complexes; Hosoi et al., 2009; Kim and von Gersdorff, 2009). Instead, our results suggest that endocytosis maintains fusion competence by acting at later steps in the fusion process. Inhibiting endocytosis is more likely to disrupt the arrangement of plasma membrane–associated proteins than vesicle-associated proteins. Plasma membrane–associated t-SNAREs are therefore good candidates for proteins rendered dysfunctional by inhibition of endocytosis. The t-SNARE syntaxin is needed for both docking and release (Südhof, 2013). Syntaxin is located on the presynaptic plasma membrane, where it tends to cluster at active zones (Lang et al., 2001; Sieber et al., 2007; Barg et al., 2010; Ribrault et al., 2011; Bar-On et al., 2012). This clustering requires PI 3,4,5 trisphosphate (PI(3,4,5)P$_3$; van den Bogaart et al., 2011; Khuong et al., 2013). Deposition of lipids and proteins from a prior vesicle fusion event might transiently disrupt this clustering by altering the local distribution of PI(3,4,5)P$_3$ and syntaxin (Ullrich et al., 2015). SNAP-25 clusters (Lang et al., 2001; Bar-On et al., 2012) might also be disrupted by prior fusion. The presence of specific protein isoforms shape the processes of docking, priming, and fusion at different synapses (Kasai et al., 2012), and so the particular proteins expressed at rod ribbon synapses might contribute to their particular sensitivity to inhibition of endocytosis. For example, unlike conventional synapses that typically use syntaxin-1, photoreceptor ribbons use syntaxin-3B (Curtis et al., 2008, 2010), and SNARE complex formation at retinal ribbon synapses is regulated by phosphorylation of syntaxin 3B by Ca^{2+}/calmodulin-dependent kinase II (Curtis et al., 2010). If inhibiting endocytosis were to somehow disrupt this critical interaction, it would impair SNARE complex formation.

The relatively depolarized resting membrane potential maintained by rod photoreceptors promotes continuous multivesicular release. The sensitivity to inhibition of endocytosis indicates that this process of multivesicular release from rod ribbons occurs at focal sites within a compact active zone. The proximity of many release sites to one another beneath a ribbon makes the need for rapid and robust endocytosis particularly critical in maintaining the integrity and structure of the active zone at photoreceptor ribbon synapses. This is, in turn, essential for accurately regulating synaptic release rates in response to illumination-dependent changes in rod membrane potential, thereby encoding the visual information collected by phototransduction in rod outer segments.

Acknowledgments

References

Alcor, D., G. Gouzer, and A. Triller. 2009. Single-particle tracking methods for the study of membrane receptors dynamics. *Eur. J. Neurosci.* 30:987–997. https://doi.org/10.1111/j.1460-9568.2009.06927.x

Armstrong-Gold, C.E., and F. Rieke. 2003. Bandpass filtering at the rod to second-order cell synapse in salamander (*Ambystoma tigrinum*) retina. *J. Neurosci.* 23:3796–3806.

Babai, N., T.M. Bartoletti, and W.B. Thoreson. 2010. Calcium regulates vesicle replenishment at the cone ribbon synapse. *J. Neurosci.* 30:15866–15877. https://doi.org/10.1523/JNEUROSCI.2891-10.2010

Bannai, H., S. Lévi, C. Schweizer, M. Dahan, and A. Triller. 2006. Imaging the lateral diffusion of membrane molecules with quantum dots. *Nat. Protoc.* 1:2628–2634. https://doi.org/10.1038/nprot.2006.429

Barg, S., M.K. Knowles, X. Chen, M. Midorikawa, and W. Almers. 2010. Syntaxin clusters assemble reversibly at sites of secretory granules in live cells. *Proc. Natl. Acad. Sci. USA.* 107:20804–20809. https://doi.org/10.1073/pnas.1014823107

Bar-On, D., S. Wolter, S. van de Linde, M. Heilemann, G. Nudelman, E. Nachliel, M. Gutman, M. Sauer, and U. Ashery. 2012. Super-resolution imaging reveals the internal architecture of nano-sized syntaxin clusters. *J. Biol. Chem.* 287:27158–27167. https://doi.org/10.1074/jbc.M112.353250

Bartoletti, T.M., and W.B. Thoreson. 2011. Quantal amplitude at the cone ribbon synapse can be adjusted by changes in cytosolic glutamate. *Mol. Vis.* 17:920–931.

Bartoletti, T.M., N. Babai, and W.B. Thoreson. 2010. Vesicle pool size at the salamander cone ribbon synapse. *J. Neurophysiol.* 103:419–423. https://doi.org/10.1152/jn.00718.2009

Bartoletti, T.M., S.L. Jackman, N. Babai, A.J. Mercer, R.H. Kramer, and W.B. Thoreson. 2011. Release from the cone ribbon synapse under bright light conditions can be controlled by the opening of only a few Ca(2+) channels. *J. Neurophysiol.* 106:2922–2935. https://doi.org/10.1152/jn.00634.2011

Cadetti, L., D. Tranchina, and W.B. Thoreson. 2005. A comparison of release kinetics and glutamate receptor properties in shaping rod-cone differences in EPSC kinetics in the salamander retina. *J. Physiol.* 569:773–788. https://doi.org/10.1113/jphysiol.2005.096545

Cadetti, L., E.J. Bryson, C.A. Ciccone, K. Rabl, and W.B. Thoreson. 2006. Calcium-induced calcium release in rod photoreceptor terminals boosts synaptic transmission during maintained depolarization. *Eur. J. Neurosci.* 23:2983–2990. https://doi.org/10.1111/j.1460-9568.2006.04845.x

Chen, M., M.J. Van Hook, D. Zenisek, and W.B. Thoreson. 2013. Properties of ribbon and non-ribbon release from rod photoreceptors revealed by visualizing individual synaptic vesicles. *J. Neurosci.* 33:2071–2086. https://doi.org/10.1523/JNEUROSCI.3426-12.2013

Chen, M., D. Križaj, and W.B. Thoreson. 2014. Intracellular calcium stores drive slow non-ribbon vesicle release from rod photoreceptors. *Front. Cell. Neurosci.* 8:20. https://doi.org/10.3389/fncel.2014.00020

Cork, K.M., and W.B. Thoreson. 2014. Rapid kinetics of endocytosis at rod photoreceptor synapses depends upon endocytic load and calcium. *Vis. Neurosci.* 31:227–235. https://doi.org/10.1017/S095252381400011X

Cork, K.M., M.J. Van Hook, and W.B. Thoreson. 2016. Mechanisms, pools, and sites of spontaneous vesicle release at synapses of rod and cone photoreceptors. *Eur. J. Neurosci.* 44:2015–2027.

Courty, S., C. Bouzigues, C. Luccardini, M.V. Ehrensperger, S. Bonneau, and M. Dahan. 2006. Tracking individual proteins in living cells using single quantum dot imaging. *Methods Enzymol.* 414:211–228. https://doi.org/10.1016/S0076-6879(06)14012-4

Crawford, D.C., and E.T. Kavalali. 2015. Molecular underpinnings of synaptic vesicle pool heterogeneity. *Traffic.* 16:338–364. https://doi.org/10.1111/tra.12262

Curtis, L.B., B. Doneske, X. Liu, C. Thaller, J.A. McNew, and R. Janz. 2008. Syntaxin 3b is a t-SNARE specific for ribbon synapses of the retina. *J. Comp. Neurol.* 510:550–559. https://doi.org/10.1002/cne.21806

Curtis, L., P. Datta, X. Liu, N. Bogdanova, R. Heidelberger, and R. Janz. 2010. Syntaxin 3B is essential for the exocytosis of synaptic vesicles in ribbon synapses of the retina. *Neuroscience.* 166:832–841. https://doi.org/10.1016/j.neuroscience.2009.12.075

Davies, A., I. Kadurin, A. Alvarez-Laviada, L. Douglas, M. Nieto-Rostro, C.S. Bauer, W.S. Pratt, and A.C. Dolphin. 2010. The alpha2delta subunits of voltage-gated calcium channels form GPI-anchored proteins, a posttranslational modification essential for function. *Proc. Natl. Acad. Sci. USA.* 107:1654–1659. https://doi.org/10.1073/pnas.0908735107

Douthitt, H.L., F. Luo, S.D. McCann, and S.D. Meriney. 2011. Dynasore, an inhibitor of dynamin, increases the probability of transmitter release. *Neuroscience.* 172:187–195. https://doi.org/10.1016/j.neuroscience.2010.10.002

Eggermann, E., I. Bucurenciu, S.P. Goswami, and P. Jonas. 2011. Nanodomain coupling between Ca²⁺ channels and sensors of exocytosis at fast mammalian synapses. *Nat. Rev. Neurosci.* 13:7–21. https://doi.org/10.1038/nrn3125

Francis, A.A., B. Mehta, and D. Zenisek. 2011. Development of new peptide-based tools for studying synaptic ribbon function. *J. Neurophysiol.* 106:1028–1037. https://doi.org/10.1152/jn.00255.2011

Fuchs, M., J.H. Brandstätter, and H. Regus-Leidig. 2014. Evidence for a Clathrin-independent mode of endocytosis at a continuously active sensory synapse. *Front. Cell. Neurosci.* 8:60. https://doi.org/10.3389/fncel.2014.00060

Girard, E., J.L. Paul, N. Fournier, P. Beaune, L. Johannes, C. Lamaze, and B. Védie. 2011. The dynamin chemical inhibitor dynasore impairs cholesterol trafficking and sterol-sensitive genes transcription in human HeLa cells and macrophages. *PLoS One.* 6:e29042. https://doi.org/10.1371/journal.pone.0029042

Grabner, C.P., C.P. Ratliff, A.C. Light, and S.H. DeVries. 2016. Mechanism of high-frequency signaling at a depressing ribbon synapse. *Neuron.* 91:133–145. https://doi.org/10.1016/j.neuron.2016.05.019

Grabs, D., V.I. Slepnev, Z. Songyang, C. David, M. Lynch, L.C. Cantley, and P. De Camilli. 1997. The SH3 domain of amphiphysin binds the proline-rich domain of dynamin at a single site that defines a new SH3 binding consensus sequence. *J. Biol. Chem.* 272:13419–13425. https://doi.org/10.1074/jbc.272.20.13419

Graydon, C.W., S. Cho, G.L. Li, B. Kachar, and H. von Gersdorff. 2011. Sharp Ca²⁺ nanodomains beneath the ribbon promote highly synchronous multivesicular release at hair cell synapses. *J. Neurosci.* 31:16637–16650. https://doi.org/10.1523/JNEUROSCI.1866-11.2011

Hall, D. 2008. Analysis and interpretation of two-dimensional single-particle tracking microscopy measurements: effect of local surface roughness. *Anal. Biochem.* 377:24–32. https://doi.org/10.1016/j.ab.2008.02.019

Hori, T., and T. Takahashi. 2012. Kinetics of synaptic vesicle refilling with neurotransmitter glutamate. *Neuron.* 76:511–517. https://doi.org/10.1016/j.neuron.2012.08.013

Hosoi, N., M. Holt, and T. Sakaba. 2009. Calcium dependence of exo- and endocytotic coupling at a glutamatergic synapse. *Neuron.* 63:216–229. https://doi.org/10.1016/j.neuron.2009.06.010

Hua, Y., A. Woehler, M. Kahms, V. Haucke, E. Neher, and J. Klingauf. 2013. Blocking endocytosis enhances short-term synaptic depression under conditions of normal availability of vesicles. *Neuron.* 80:343–349. https://doi.org/10.1016/j.neuron.2013.08.010

Innocenti, B., and R. Heidelberger. 2008. Mechanisms contributing to tonic release at the cone photoreceptor ribbon synapse. *J. Neurophysiol.* 99:25–36. https://doi.org/10.1152/jn.00737.2007

Jackman, S.L., S.Y. Choi, W.B. Thoreson, K. Rabl, T.M. Bartoletti, and R.H. Kramer. 2009. Role of the synaptic ribbon in transmitting the cone light response. *Nat. Neurosci.* 12:303–310. https://doi.org/10.1038/nn.2267

Jockusch, W.J., G.J. Praefcke, H.T. McMahon, and L. Lagnado. 2005. Clathrin-dependent and clathrin-independent retrieval of synaptic vesicles in retinal bipolar cells. *Neuron.* 46:869–878. https://doi.org/10.1016/j.neuron.2005.05.004

Johnson, S.L., J. Olt, S. Cho, H. von Gersdorff, and W. Marcotti. 2017. The coupling between Ca²⁺ channels and the exocytotic Ca²⁺ sensor at hair cell ribbon synapses varies tonotopically along the mature cochlea. *J. Neurosci.* 37:2471–2484. https://doi.org/10.1523/JNEUROSCI.2867-16.2017

Kasai, H., N. Takahashi, and H. Tokumaru. 2012. Distinct initial SNARE configurations underlying the diversity of exocytosis. *Physiol. Rev.* 92:1915–1964. https://doi.org/10.1152/physrev.00007.2012

Kawasaki, F., M. Hazen, and R.W. Ordway. 2000. Fast synaptic fatigue in shibire mutants reveals a rapid requirement for dynamin in synaptic vesicle membrane trafficking. *Nat. Neurosci.* 3:859–860. https://doi.org/10.1038/78753

Khuong, T.M., R.L. Habets, S. Kuenen, A. Witkowska, J. Kasprowicz, J. Swerts, R. Jahn, G. van den Bogaart, and P. Verstreken. 2013. Synaptic PI(3,4,5)P3 is required for Syntaxin1A clustering and neurotransmitter release. *Neuron.* 77:1097–1108. https://doi.org/10.1016/j.neuron.2013.01.025

Kim, J.H., and H. von Gersdorff. 2009. Traffic jams during vesicle cycling lead to synaptic depression. *Neuron.* 63:143–145. https://doi.org/10.1016/j.neuron.2009.07.006

Krizaj, D., J.X. Bao, Y. Schmitz, P. Witkovsky, and D.R. Copenhagen. 1999. Caffeine-sensitive calcium stores regulate synaptic transmission from retinal rod photoreceptors. *J. Neurosci.* 19:7249–7261.

Kusumi, A., Y. Sako, and M. Yamamoto. 1993. Confined lateral diffusion of membrane receptors as studied by single particle tracking (nanovid microscopy). Effects of calcium-induced differentiation in cultured epithelial cells. *Biophys. J.* 65:2021–2040. https://doi.org/10.1016/S0006-3495(93)81253-0

Lang, T., D. Bruns, D. Wenzel, D. Riedel, P. Holroyd, C. Thiele, and R. Jahn. 2001. SNAREs are concentrated in cholesterol-dependent clusters that define docking and fusion sites for exocytosis. *EMBO J.* 20:2202–2213. https://doi.org/10.1093/emboj/20.9.2202

Lasansky, A. 1978. Contacts between receptors and electrophysiologically identified neurones in the retina of the larval tiger salamander. *J. Physiol.* 285:531–542. https://doi.org/10.1113/jphysiol.1978.sp012587

Lipstein, N., T. Sakaba, B.H. Cooper, K.H. Lin, N. Strenzke, U. Ashery, J.S. Rhee, H. Taschenberger, E. Neher, and N. Brose. 2013. Dynamic

control of synaptic vesicle replenishment and short-term plasticity by Ca(2+)-calmodulin-Munc13-1 signaling. *Neuron.* 79:82–96. https://doi.org/10.1016/j.neuron.2013.05.011

LoGiudice, L., and G. Matthews. 2009. The role of ribbons at sensory synapses. *Neuroscientist.* 15:380–391. https://doi.org/10.1177/1073858408331373

Logiudice, L., P. Sterling, and G. Matthews. 2009. Vesicle recycling at ribbon synapses in the finely branched axon terminals of mouse retinal bipolar neurons. *Neuroscience.* 164:1546–1556. https://doi.org/10.1016/j.neuroscience.2009.09.023

Lv, C., T.J. Gould, J. Bewersdorf, and D. Zenisek. 2012. High-resolution optical imaging of zebrafish larval ribbon synapse protein RIBEYE, RIM2, and CaV 1.4 by stimulation emission depletion microscopy. *Microsc. Microanal.* 18:745–752. https://doi.org/10.1017/S1431927612000268

Mahapatra, S., F. Fan, and X. Lou. 2016. Tissue-specific dynamin-1 deletion at the calyx of Held decreases short-term depression through a mechanism distinct from vesicle resupply. *Proc. Natl. Acad. Sci. USA.* 113:E3150–E3158. https://doi.org/10.1073/pnas.1520937113

Maple, B.R., F.S. Werblin, and S.M. Wu. 1994. Miniature excitatory postsynaptic currents in bipolar cells of the tiger salamander retina. *Vision Res.* 34:2357–2362. https://doi.org/10.1016/0042-6989(94)90281-X

McCluskey, A., J.A. Daniel, G. Hadzic, N. Chau, E.L. Clayton, A. Mariana, A. Whiting, N.N. Gorgani, J. Lloyd, A. Quan, et al. 2013. Building a better dynasore: the dyngo compounds potently inhibit dynamin and endocytosis. *Traffic.* 14:1272–1289. https://doi.org/10.1111/tra.12119

Mehta, B., J. Snellman, S. Chen, W. Li, and D. Zenisek. 2013. Synaptic ribbons influence the size and frequency of miniature-like evoked postsynaptic currents. *Neuron.* 77:516–527. https://doi.org/10.1016/j.neuron.2012.11.024

Mercer, A.J., and W.B. Thoreson. 2013. Tracking quantum dot–tagged calcium channels at vertebrate photoreceptor synapses: retinal slices and dissociated cells. *In* Current Protocols in Neuroscience. C. Gerfen, A. Holmes, D. Sibley, P. Skolnick, and S. Wray, editors. Wiley, New York. 2.18.1–2.18.23.

Mercer, A.J., M. Chen, and W.B. Thoreson. 2011. Lateral mobility of presynaptic L-type calcium channels at photoreceptor ribbon synapses. *J. Neurosci.* 31:4397–4406. https://doi.org/10.1523/JNEUROSCI.5921-10.2011

Mercer, A.J., R.J. Szalewski, S.L. Jackman, M.J. Van Hook, and W.B. Thoreson. 2012. Regulation of presynaptic strength by controlling Ca²⁺ channel mobility: effects of cholesterol depletion on release at the cone ribbon synapse. *J. Neurophysiol.* 107:3468–3478. https://doi.org/10.1152/jn.00779.2011

Moser, T., and D. Beutner. 2000. Kinetics of exocytosis and endocytosis at the cochlear inner hair cell afferent synapse of the mouse. *Proc. Natl. Acad. Sci. USA.* 97:883–888. https://doi.org/10.1073/pnas.97.2.883

Nachman-Clewner, M., R. St Jules, and E. Townes-Anderson. 1999. L-type calcium channels in the photoreceptor ribbon synapse: localization and role in plasticity. *J. Comp. Neurol.* 415:1–16. https://doi.org/10.1002/(SICI)1096-9861(19991206)415:1%3C1::AID-CNE1%3E3.0.CO;2-G

Neher, E. 2010. What is rate-limiting during sustained synaptic activity: Vesicle Supply or the availability of release sites. *Front. Synaptic Neurosci.* 2:144. https://doi.org/10.3389/fnsyn.2010.00144

Neher, E. 2017. Some Subtle Lessons from the Calyx of Held Synapse. *Biophys. J.* 112:215–223. https://doi.org/10.1016/j.bpj.2016.12.017

Park, R.J., H. Shen, L. Liu, X. Liu, S.M. Ferguson, and P. De Camilli. 2013. Dynamin triple knockout cells reveal off target effects of commonly used dynamin inhibitors. *J. Cell Sci.* 126:5305–5312. https://doi.org/10.1242/jcs.138578

Parsons, T.D., D. Lenzi, W. Almers, and W.M. Roberts. 1994. Calcium-triggered exocytosis and endocytosis in an isolated presynaptic cell: capacitance measurements in saccular hair cells. *Neuron.* 13:875–883. https://doi.org/10.1016/0896-6273(94)90253-4

Preta, G., J.G. Cronin, and I.M. Sheldon. 2015. Dynasore - not just a dynamin inhibitor. *Cell Commun. Signal.* 13:24. https://doi.org/10.1186/s12964-015-0102-1

Qin, N., S. Yagel, M.L. Momplaisir, E.E. Codd, and M.R. D'Andrea. 2002. Molecular cloning and characterization of the human voltage-gated calcium channel alpha(2)delta-4 subunit. *Mol. Pharmacol.* 62:485–496. https://doi.org/10.1124/mol.62.3.485

Rabl, K., L. Cadetti, and W.B. Thoreson. 2006. Paired-pulse depression at photoreceptor synapses. *J. Neurosci.* 26:2555–2563. https://doi.org/10.1523/JNEUROSCI.3667-05.2006

Ribrault, C., J. Reingruber, M. Petković, T. Galli, N.E. Ziv, D. Holcman, and A. Triller. 2011. Syntaxin1A lateral diffusion reveals transient and local SNARE interactions. *J. Neurosci.* 31:17590–17602. https://doi.org/10.1523/JNEUROSCI.4065-11.2011

Robinson, P., S. Etheridge, L. Song, R. Shah, E.M. Fitzgerald, and O.T. Jones. 2011. Targeting of voltage-gated calcium channel α2δ-1 subunit to lipid rafts is independent from a GPI-anchoring motif. *PLoS One.* 6:e19802. https://doi.org/10.1371/journal.pone.0019802

Schmitz, F. 2009. The making of synaptic ribbons: how they are built and what they do. *Neuroscientist.* 15:611–624. https://doi.org/10.1177/1073858409340253

Schnee, M.E., J. Santos-Sacchi, M. Castellano-Muñoz, J.H. Kong, and A.J. Ricci. 2011. Calcium-dependent synaptic vesicle trafficking underlies indefatigable release at the hair cell afferent fiber synapse. *Neuron.* 70:326–338. https://doi.org/10.1016/j.neuron.2011.01.031

Sieber, J.J., K.I. Willig, C. Kutzner, C. Gerding-Reimers, B. Harke, G. Donnert, B. Rammner, C. Eggeling, S.W. Hell, H. Grubmüller, and T. Lang. 2007. Anatomy and dynamics of a supramolecular membrane protein cluster. *Science.* 317:1072–1076. https://doi.org/10.1126/science.1141727

Snellman, J., B. Mehta, N. Babai, T.M. Bartoletti, W. Akmentin, A. Francis, G. Matthews, W. Thoreson, and D. Zenisek. 2011. Acute destruction of the synaptic ribbon reveals a role for the ribbon in vesicle priming. *Nat. Neurosci.* 14:1135–1141. https://doi.org/10.1038/nn.2870

Südhof, T.C. 2013. Neurotransmitter release: the last millisecond in the life of a synaptic vesicle. *Neuron.* 80:675–690. https://doi.org/10.1016/j.neuron.2013.10.022

Suryanarayanan, A., and M.M. Slaughter. 2006. Synaptic transmission mediated by internal calcium stores in rod photoreceptors. *J. Neurosci.* 26:1759–1766. https://doi.org/10.1523/JNEUROSCI.3895-05.2006

Taschenberger, H., R.M. Leão, K.C. Rowland, G.A. Spirou, and H. von Gersdorff. 2002. Optimizing synaptic architecture and efficiency for high-frequency transmission. *Neuron.* 36:1127–1143. https://doi.org/10.1016/S0896-6273(02)01137-6

Thoreson, W.B., K. Rabl, E. Townes-Anderson, and R. Heidelberger. 2004. A highly Ca²⁺-sensitive pool of vesicles contributes to linearity at the rod photoreceptor ribbon synapse. *Neuron.* 42:595–605. https://doi.org/10.1016/S0896-6273(04)00254-5

Thoreson, W.B., A.J. Mercer, K.M. Cork, and R.J. Szalewski. 2013. Lateral mobility of L-type calcium channels in synaptic terminals of retinal bipolar cells. *Mol. Vis.* 19:16–24.

Thoreson, W.B., M.J. Van Hook, C. Parmelee, and C. Curto. 2016. Modeling and measurement of vesicle pools at the cone ribbon synapse: Changes in release probability are solely responsible for voltage-dependent changes in release. *Synapse.* 70:1–14. https://doi.org/10.1002/syn.21871

Townes-Anderson, E., P.R. MacLeish, and E. Raviola. 1985. Rod cells dissociated from mature salamander retina: ultrastructure and uptake of horseradish peroxidase. *J. Cell Biol.* 100:175–188. https://doi.org/10.1083/jcb.100.1.175

Ullrich, A., M.A. Böhme, J. Schöneberg, H. Depner, S.J. Sigrist, and F. Noé. 2015. Dynamical organization of syntaxin-1A at the presynaptic active zone. *PLOS Comput. Biol.* 11:e1004407. https://doi.org/10.1371/journal.pcbi.1004407

Vaithianathan, T., and G. Matthews. 2014. Visualizing synaptic vesicle turnover and pool refilling driven by calcium nanodomains at presynaptic active zones of ribbon synapses. *Proc. Natl. Acad. Sci. USA.* 111:8655–8660. https://doi.org/10.1073/pnas.1323962111

van den Bogaart, G., K. Meyenberg, H.J. Risselada, H. Amin, K.I. Willig, B.E. Hubrich, M. Dier, S.W. Hell, H. Grubmüller, U. Diederichsen, and R. Jahn. 2011. Membrane protein sequestering by ionic protein-lipid interactions. *Nature.* 479:552–555. https://doi.org/10.1038/nature10545

Van Hook, M.J., and W.B. Thoreson. 2012. Rapid synaptic vesicle endocytosis in cone photoreceptors of salamander retina. *J. Neurosci.* 32:18112–18123. https://doi.org/10.1523/JNEUROSCI.1764-12.2012

Van Hook, M.J., and W.B. Thoreson. 2013. Simultaneous whole-cell recordings from photoreceptors and second-order neurons in an amphibian retinal slice preparation. *J. Vis. Exp.* 76:50007.

Van Hook, M.J., and W.B. Thoreson. 2014. Endogenous calcium buffering at photoreceptor synaptic terminals in salamander retina. *Synapse.* 68:518–528. https://doi.org/10.1002/syn.21768

Van Hook, M.J., and W.B. Thoreson. 2015. Weak endogenous Ca²⁺ buffering supports sustained synaptic transmission by distinct mechanisms in rod and cone photoreceptors in salamander retina. *Physiol. Rep.* 3:e12567. https://doi.org/10.14814/phy2.12567

Van Hook, M.J., C.M. Parmelee, M. Chen, K.M. Cork, C. Curto, and W.B. Thoreson. 2014. Calmodulin enhances ribbon replenishment and shapes filtering of synaptic transmission by cone photoreceptors. *J. Gen. Physiol.* 144:357–378. https://doi.org/10.1085/jgp.201411229

Verhage, M., and J.B. Sørensen. 2008. Vesicle docking in regulated exocytosis. *Traffic.* 9:1414–1424. https://doi.org/10.1111/j.1600-0854.2008.00759.x

von Gersdorff, H., and G. Matthews. 1994. Inhibition of endocytosis by elevated internal calcium in a synaptic terminal. *Nature.* 370:652–655. https://doi.org/10.1038/370652a0

Wahl, S., R. Katiyar, and F. Schmitz. 2013. A local, periactive zone endocytic machinery at photoreceptor synapses in close vicinity to synaptic ribbons. *J. Neurosci.* 33:10278–10300. https://doi.org/10.1523/JNEUROSCI.5048-12.2013

Wen, X., G.W. Saltzgaber, and W.B. Thoreson. 2017. Kiss-and-run is a significant contributor to synaptic exocytosis and endocytosis in photoreceptors. *Front. Cell. Neurosci.* 11:286. https://doi.org/10.3389/fncel.2017.00286

Zenisek, D., N.K. Horst, C. Merrifield, P. Sterling, and G. Matthews. 2004. Visualizing synaptic ribbons in the living cell. *J. Neurosci.* 24:9752–9759. https://doi.org/10.1523/JNEUROSCI.2886-04.2004